El Niño Flavors and Their Simulated Impacts on Atmospheric Circulation in the High Southern Latitudes*

AARON B. WILSON

Polar Meteorology Group, Byrd Polar Research Center, The Ohio State University, Columbus, Ohio

DAVID H. BROMWICH

Polar Meteorology Group, Byrd Polar Research Center, and Atmospheric Sciences Program, Department of Geography, The Ohio State University, Columbus, Ohio

KEITH M. HINES AND SHENG-HUNG WANG

Polar Meteorology Group, Byrd Polar Research Center, The Ohio State University, Columbus, Ohio

(Manuscript received 23 April 2014, in final form 29 August 2014)

ABSTRACT

Two El Niño flavors have been defined based on whether warm sea surface temperature (SST) anomalies are located in the central or eastern tropical Pacific (CP or EP). This study further characterizes the impacts on atmospheric circulation in the high latitudes of the Southern Hemisphere associated with these types of El Niño events though a series of numerical simulations using the National Center for Atmospheric Research Community Atmosphere Model (CAM). Comparing results with the Interim ECMWF Re-Analysis (ERA-Interim), CAM simulates well the known changes to blocking over Australia and a southward shift in the subtropical jet stream across the eastern Pacific basin during CP events. More importantly for the high southern latitudes, CAM simulates a westward shift in upper-level divergence in the tropical Pacific, which causes the Pacific–South American stationary wave pattern to shift toward the west across the entire South Pacific. These changes to the Rossby wave source region impact the South Pacific convergence zone and jet streams and weaken the high-latitude blocking that is typically present in the Amundsen-Bellingshausen Seas during EP events. Anticyclonic flow becomes established farther west in the south central Pacific, modifying high-latitude heat and momentum fluxes across the South Pacific and South Atlantic associated with the ENSO–Antarctic dipole.

1. Introduction

The onset and development of El Niño–Southern Oscillation (ENSO) in the tropical Pacific Ocean are monitored in four key regions ranging from the western Pacific to the South American coast: Niño-4: 5°N–5°S, 160°E–150°W; Niño-3.4: 5°N–5°S, 170°–120°W; Niño-3: 5°N–5°S, 150°–90°W; and Niño-1+2: 0°–10°S, 90°–80°W. Focus has historically been on the Niño-3.4 or Niño-3 regions and anomalous sea surface temperatures (SSTs) within each box meeting a threshold above or below the climate base period (Trenberth 1997). However, tropical Pacific SST anomalies are not uniformly captured by a single index including Niño-3.4, with anomalous activity occurring at times throughout the entire eastern tropical Pacific while at other times activity is more centralized in the tropical Pacific. An effort to distinguish ENSO types by the location of the maximum SST anomalies in the tropical Pacific has given rise to ENSO ''flavors,'' subtle variations in the characteristics of ENSO that affect teleconnections to remote regions of the globe.

Larkin and Harrison (2005) identified ''dateline El Niños,'' events whose strongest SST warming occur only in the central tropical Pacific near the international date

* Byrd Polar Research Center Contribution Number 1451.

Corresponding author address: Aaron B. Wilson, Polar Meteorology Group, Byrd Polar Research Center, The Ohio State University, 1090 Carmack Road, Columbus, OH 43210.
E-mail: wilson.1010@osu.edu

DOI: 10.1175/JCLI-D-14-00296.1

line. Similarly, Ashok et al. (2007) used the second leading mode of tropical Pacific SST anomalies to identify ''ENSO Modoki,'' an event with the ascending branch of the Walker circulation in the central Pacific and descending branches on either side. Compared to the classic type associated with a warm tongue of SSTs extending from the South American coast, El Niño Modoki exhibits cooler SSTs and less convection in the eastern tropical Pacific. Kao and Yu (2009) and Yu and Kim (2010) use a method combining empirical orthogonal function analysis and linear regression to produce an eastern Pacific (EP) and central Pacific (CP) index, while Kug et al. (2009, 2010) use SST differences between the Niño-4 and Niño-3 basins, referring to events as warm pool (WP) and cold tongue (CT) events.

Much of the research on El Niño flavors has focused on tropical and subtropical impacts with little attention paid to the high latitudes. Concurrently, extensive research concerning ENSO forcing of transient eddy activity (Seager et al. 2003; L'Heureux and Thompson 2006; Fogt and Bromwich 2006; Fogt et al. 2011), changes to the asymmetric Rossby waves (Ding et al. 2012), anticyclonic wave breaking on the equator side of the eddy-driven jet (Gong et al. 2010, 2013), and the modulation of the tropical influence by the southern annular mode (SAM) (Fogt et al. 2011) has provided insights into the individual and coupled impacts of ENSO and SAM on high-latitude atmospheric circulation. However, only Ding et al. (2012) allude to El Niño flavors by addressing seasonal tropical SST trends without directly addressing dynamical differences between El Niño types. Therefore, it is important to evaluate changes to atmospheric circulation in the high southern latitudes due to El Niño flavors so the dynamical coupling between ENSO and SAM may be better understood.

Although uncertainty remains as to the development and growth phases of CP El Niños in coupled climate models (Capotondi 2013), Yeh et al. (2009) have used future global warming scenarios depicted by phase 3 of the Coupled Model Intercomparison Project (CMIP3) to show that the ratio of CP versus EP El Niños is likely to increase. Already, the last three decades have witnessed an increase in the frequency (Ashok et al. 2007) and intensity (Lee and McPhaden 2010) of CP El Niño events. The increased frequency of CP events has been linked to sea level pressure variations in the North Pacific induced by a strengthening of the Hadley circulation (Yu et al. 2012). Since the climate of West Antarctica is extremely sensitive to atmospheric changes over the South Pacific Ocean (Nicolas and Bromwich 2011; Bromwich et al. 2013), and given the accelerated ice flow from outlet glaciers (e.g., Pine Island and Thwaites) due to the thinning of floating ice shelves (Jenkins et al. 2010; Jacobs et al. 2011), it is important to understand how ENSO flavors in a warming world may impact atmospheric circulation variability in this region, including changes that may induce a continued increase in the rate of global sea level rise from West Antarctica.

There are clear obstacles inherent to observing El Niño flavors (limited frequency of events and varying strengths of each type) that make understanding their effects on atmospheric circulation challenging. To aid in this endeavor, this study takes advantage of a global atmospheric model, whereby SSTs defined by each El Niño flavor are repeated and the atmospheric response in the model is evaluated. First, by comparing changes in atmospheric circulation between the National Center for Atmospheric Research (NCAR) Community Atmosphere Model (CAM) and the Interim European Centre for Medium-Range Weather Forecasts (ECMWF) ReAnalysis (ERA-Interim, herein ERAI), the reliability of the CAM model to represent these changes is tested. Second, by imposing equal amplitudes for each type, the resultant atmospheric circulation patterns including changes to jet streams and stationary eddies throughout the South Pacific and high-southern latitudes are linked directly to the spatial differences between CP and EP El Niño events.

The paper is organized as follows. Section 2 describes the global model and analysis techniques used to evaluate El Niño flavors. Section 3 demonstrates how the lower boundary conditions for each type are constructed, specifically the SST variability differences between two El Niño flavors. Section 4 details the overall differences in atmospheric circulation in the high southern latitudes during each type of El Niño, and section 5 highlights differences between their zonal-mean zonal wind and jet stream positions in the Pacific Ocean. Section 6 illustrates changes to the stationary eddy pattern across the South Pacific and section 7 summarizes the findings.

2. Data and methodology

a. Community Atmosphere Model

The NCAR Community Atmosphere Model version 4 (Neale et al. 2010) was used for model simulations in this study after extensive testing found CAM suitable for ENSO simulations (Wilson 2013). CAM was developed by the Atmosphere Model Working Group at NCAR, and version 4 was released in June 2010 as a stand-alone model or as a component of the fully coupled Community Climate System Model version 4 (CCSM4; Gent et al. 2011) in preparation for the Intergovernmental Panel on Climate Change (IPCC) Fifth Assessment

Report. The stand-alone version of CAM has an atmospheric model coupled to an active land model (NCAR Community Land Model). The lower boundary conditions [SSTs and sea ice concentrations (SICs)] are prescribed using a dataset designed for uncoupled CAM simulations (Hurrell et al. 2008). This dataset combines the monthly mean Hadley Centre Sea Ice and Sea Surface Temperature dataset version 1.1 (HadISST1; Rayner et al. 2003) with version 2 of the National Oceanic and Atmospheric Administration (NOAA) weekly optimum interpolation SST (OI.v2) analysis (Reynolds et al. 2002). Details pertinent to the construction of prescribed SSTs for each El Niño flavor are provided in section 3. Ozone and carbon dioxide concentrations for all simulations were based on observations. The radiation parameterization used monthly-mean ozone volume mixing ratios that are specified as a function of latitude, vertical pressure level, and time (Neale et al. 2010). Orbital parameters were set to 1990 levels, and climatological aerosol concentrations were used.

Simulations were performed using the spectral Eulerian dynamical core with 26 vertical levels and an 85-wave triangular truncation (T85L26, 128 × 256 horizontal grid) with an equivalent resolution of 1.4°. CAM uses a hybrid vertical coordinate system (Simmons and Strüfing 1981) that is terrain-following near Earth's surface with a hybrid sigma-pressure region above and a fixed upper boundary pressure surface (~3 hPa). CAM simulates atmospheric circulation and tropical interannual variability well (Hurrell et al. 2006) whereas tropical intraseasonal variability has historically been a challenge due to errors in the convection scheme (Neale et al. 2008). Modifications to the convective momentum transport and a convective available potential energy dilution approximation in newer versions of CAM (included in version 4) have improved intraseasonal variability and weakened model trade winds, allowing for a better representation of ENSO (Neale et al. 2008).

b. ERA-Interim

The ERAI (Dee et al. 2011) is used to verify atmospheric circulation changes during different flavors of El Niño from 1979–2010. ERAI has an advantage over other reanalyses in its use of 4D variational data assimilation and high horizontal and vertical resolutions. Recent studies have shown the superiority of ERAI over other reanalyses in the Southern Hemisphere (SH) and Antarctica for interannual variability and trends of the Antarctic surface mass balance [precipitation − evaporation ($P - E$)] from 1989 to 2009 (Bromwich et al. 2011) as well as atmospheric circulation (Bracegirdle and Marshall 2012). Using independent ice-drifting buoy observations (not included in ERAI), Bracegirdle (2013) showed that ERAI captures well the synoptic systems over the Bellingshausen Sea, providing confidence in its increasing trend of westerly winds over the nearby Amundsen Sea. Strong links between ENSO and SAM and their effects on atmospheric circulation variability have been discovered in the southeast Pacific Ocean (Fogt and Bromwich 2006; Fogt et al. 2011). Characterizing changes to the ENSO teleconnection from the tropics in ERAI allows a robust assessment of the modeled teleconnection changes in CAM that may impact the ENSO–SAM dynamic coupling.

c. Analysis techniques

Composite analysis (von Storch and Zwiers 1999) is used to express differences in mean sea level pressure (MSLP), geopotential height, and zonal wind between EP and CP events in order to identify changes to atmospheric circulation. Significance of composite differences is calculated using a t test that compares the means of the two groups. Given the t statistic and degrees of freedom, the incomplete beta function is used to calculate the probability level p that the two means are equal and are denoted in the composite figures by stippling where $p < 0.10$. This confidence level was chosen for significance based on the relatively limited number of composite cases in ERAI and the 15-yr simulation length for CAM.

To assess changes to the teleconnection to Antarctica during different flavors of El Niño in CAM, the eddy streamfunction, velocity potential, and upper-level divergent wind are used. Following Holton (1992), Helmholtz theory states that any velocity field can be decomposed into nondivergent $\mathbf{V}_\psi$ and irrotational $\mathbf{V}_\chi$ components such that

$$\mathbf{V} = \mathbf{V}_\psi + \mathbf{V}_\chi, \tag{1}$$

where $\nabla \cdot \mathbf{V}_\psi = 0$ and $\nabla \times \mathbf{V}_\chi = 0$. It follows that the nondivergent component in a two-dimensional velocity field can be expressed as a streamfunction ψ where $\mathbf{V}_\psi = \mathbf{k} \times \nabla\psi$ and represents the vorticity-related component of the flow with no divergence. The irrotational component (velocity potential) represents the divergent component of the flow and is expressed as $\mathbf{V}_\chi = \nabla\chi$. Both streamfunction and velocity potential are solved using spherical harmonics to account for the Gaussian grid. The nondivergent component of the flow follows the contours of the streamfunction and the speed of the flow is proportional to the gradient of the streamfunction.

Stationary heat and momentum fluxes in the SH are used to demonstrate high-latitude atmospheric circulation

changes during different El Niño flavors, particularly in the southeast Pacific Ocean. Following Peixoto and Oort (1992), a decomposition in time and space of the meridional and zonal components of flow gives the meridional transport of zonal momentum,

$$[\overline{vu}] = [\overline{v}][\overline{u}] + [\overline{v}^*\overline{u}^*] + [\overline{v'u'}], \quad (2)$$

and the meridional transport of heat,

$$[\overline{vT}] = [\overline{v}][\overline{T}] + [\overline{v}^*\overline{T}^*] + [\overline{v'T'}], \quad (3)$$

where the brackets denote these quantities are taken with respect to a zonal mean, the overbar represents the time (monthly) mean, the asterisk (*) represents the deviation from the zonal mean (zonal anomaly), and the prime (′) denotes the departure from the time mean (temporal anomaly). The first terms on the right-hand sides of Eqs. (2) and (3) are associated with the mean meridional fluxes of momentum and heat, the second terms represent the stationary eddies (see section 6a), and the third terms represent the transient eddies.

Expanding on earlier work by Rind et al. (2001), Yuan (2004) demonstrated that during El Niño, warm tropical Pacific SSTs induce deep convection, which strengthens the local Hadley and Ferrel cell circulation along with the subtropical jet stream (STJ) in the Pacific while weakening the polar front jet (PFJ) in the higher latitudes of the SH. The zonal (Walker) circulation in the tropics is impacted to the point of weakening the local Hadley and Ferrel cells in the western Atlantic basin, creating a seesaw relationship in the lower-level heat transport across the Antarctic Peninsula (AP) (Liu et al. 2002) known as the Antarctic dipole (ADP). This also demonstrates an important feedback between the strength of the STJ (stronger) and PFJ (weaker) to the maintenance of the anticyclonic anomaly in the Amundsen-Bellingshausen Sea (ABS) region (Renwick 1998; Renwick and Revell 1999; Revell et al. 2001) and the modulation of this behavior due to SAM (Fogt et al. 2011). Thus, changes associated with El Niño in the tropics are likely to alter the ENSO–ADP teleconnection.

3. Constructing the EP and CP simulations

a. Observed composites

CP and EP El Niño flavors were forced in our simulations through prescribed SSTs. The goal was to create tropical Pacific SSTs consistent with the spatial characteristics of CP and EP events while accounting for differences in the magnitudes of their SST anomalies and in their temporal evolution. Figure 1 shows monthly SST anomalies from 150°E to 80°W averaged from 5°S to 5°N for the period 1950–2010 using HadISST1/OI.v2. The temporal variability of the tropical Pacific SSTs is highlighted by the oscillation between cool (blue, La Niña) and warm (red, El Niño) conditions. Large EP El Niño events, such as those in 1982–83 and 1997–98, are easily detectable. Clearly there is a large degree of spatial variability for both warm and cool events, indicative of the continuum nature of ENSO. More importantly, a recent propensity for warm SST anomalies to be located in the central Pacific is apparent. For the purpose of delimiting CP and EP events, the Niño-4 and Niño-3 regions are separated in Fig. 1 by the solid black line and the western/eastern boundaries are denoted by the dotted lines for each index, respectively. Many of the early El Niño events from the 1950s through the 1980s demonstrated warm SST anomalies throughout the Niño-3 region and eastern Niño-4 region. Beginning in the early 1990s, however, positive SST anomalies have been centrally located in the tropical Pacific, with the largest anomalies generally in the Niño-4 region (with the exception of the 1997–98 event).

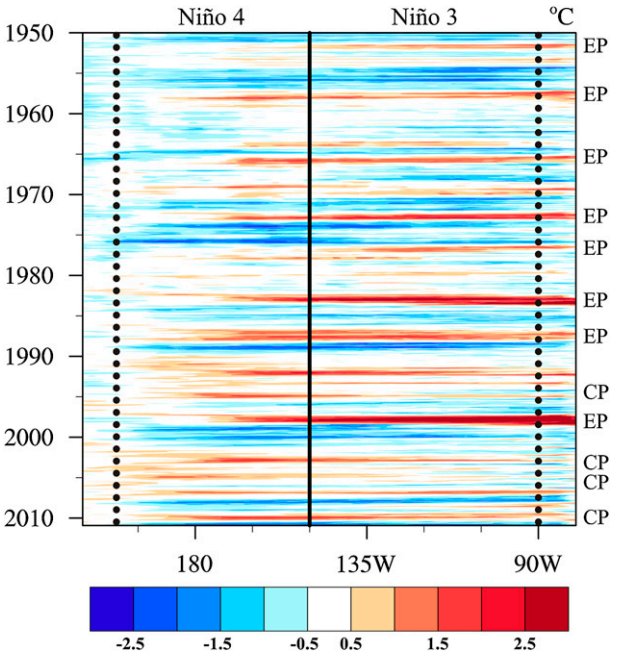

FIG. 1. Monthly SST anomalies in the tropical Pacific Ocean from 150°E to 80°W, averaged from 5°S to 5°N, and displayed as a function of time. Blue shading indicates cool (La Niña) events while red shading indicates warm (El Niño) events. The solid black line marks the boundary between the Niño-3 region in the eastern Pacific basin (right) and the Niño-4 region in the western Pacific basin (left) with the eastern and western boundaries denoted by the dotted line for each basin, respectively. EP and CP events composited for lower boundary conditions for each idealized simulation are identified and labeled on the right-hand side of the figure.

Based on Fig. 1 and a comparison of the time series anomalies from each basin, eight cases of EP El Niño events (1951–52, 1957–58, 1965–66, 1972–73, 1976–77, 1982–83, 1986–87, and 1997–98) and four cases of CP El Niño events (1994–95, 2002–03, 2004–05, and 2009–10) are used to create the lower boundary conditions in CAM. In the case of 1986–87, Ashok et al. (2007) used the El Niño Modoki index to classify this event as a CP event. As Kug et al. (2009) pointed out, however, the maximum SST anomaly for this event was located between 120° and 150°W and showed signs of a mix between the two flavors. It is included in the EP lower boundary conditions for this study because the Niño-3 index exceeds the Niño-4 index during the entire event once El Niño conditions form in October of 1986.

SSTs for all cases for each type of El Niño flavor identified in Fig. 1 during the period 1950–2010 are composited in order to create a 12-month time series ($\text{June}_{\text{before}}$–$\text{May}_{\text{after}}$ El Niño maturity) for each type. Figure 2 shows the monthly spatial anomaly composite for CP (left column) and EP (right column) events. For the EP case, warm SST anomalies are already present in the eastern Pacific by June and increase in magnitude as El Niño matures from austral spring [September–November (SON)] into austral summer [December–February (DJF)], and the trade winds weaken during this evolution. After reaching maturity in November–January, the warm SST anomalies associated with EP El Niño diminish during austral autumn [March–May (MAM)]. For the CP case, several significant differences are shown by Fig. 2. The warm SST anomalies emerge primarily in the central Pacific basin in early austral winter [June–August (JJA)] as well, but the largest anomalies remain near the date line throughout maturity. During October–February, there are positive SST anomalies in the eastern Pacific, but they are much smaller than those in the central Pacific and SST anomalies associated with the EP case. SST anomalies decrease from late DJF through MAM. CP events also demonstrate a strong response in extratropical SSTs during maturity as well (November–February), with anomalies of 1.0°–1.5°C located between 30° and 60°S and 150° and 120°W. Lee et al. (2010) showed that during the 2009–10 El Niño, the SST anomaly in the south central Pacific (SCP; 35°–55°S, 160°–110°W) exceeded five standard deviations of the SCP SST anomaly for the previous three decades and was actually greater in magnitude than the tropical Pacific SSTs associated with the Niño-4 region. To verify whether this single event is driving the extratropical anomalies present in the composites in Fig. 2, the composites were reconstructed without the 2009–10 event. Even in the absence of this large anomalous SCP event of 2009–10, the SST anomaly is still as high as 1.0°C in the SCP region (not shown). This suggests that the response in the SCP is not isolated to the 2009–10 event alone, but rather is a robust spatial signature of the CP type of El Niño events. This high-latitude impact lingers in the region throughout the decaying phase, as SST anomalies of 0.5°–1.5°C are still present into May.

Figure 2 also highlights differences in SST anomalies in the Indian and Atlantic Oceans. Small positive SST anomalies (0.5°–1.0°C) are present in the CP composites all year long although coverage is not basinwide and the magnitudes are less than those in the central Pacific. Very few SST anomalies are evident in the EP composites. The Indian Ocean SST anomalies along with the slow decay of midlatitude SST anomalies are discussed by Kim et al. (2011) for the 2009–10 CP event, as this particular El Niño transitioned quickly in the SH autumn to a La Niña event. The rapid transition was caused by an eastward wind stress due to warming in the Indian Ocean. Again, ignoring the effects of the 2009–10 event, significant SST anomalies are still present in the Indian Ocean of the CP composites (not shown), suggesting that this basin plays an important role in the decay of CP events. SST anomalies of up to 1.5°C in the Atlantic Ocean near 20°S during summer (weaker during autumn) are only reflected in the CP composites. This is likely related to the interaction between ENSO and the South Atlantic dipole (SAD) (Kayano et al. 2013), both of which affect the South American monsoon. The SAD tends to be positive in summer and autumn during warm ENSO phases, especially during CP events (Kayano and Andreoli 2006; Rodrigues et al. 2011). While SST variability in the tropical Indian and Atlantic Oceans is not the focus of this study, these differences underscore the need to understand changes in atmospheric dynamics during each type of El Niño that result in different high-latitude impacts.

b. *Idealized simulation methodology*

Given the relative magnitude differences between these two types of El Niños, composite SSTs for each are transformed to equally strong idealized cases. Normalizing these events by a strong case was done for multiple reasons. Sensitivity simulations (not shown) show that weak forcing in CAM results in variable responses compared to ERAI, the reasons for which are beyond the scope of this paper. However, matching their strengths isolates changes to the atmospheric dynamics associated with the spatial variability of each type. Research also shows an increasing trend in the occurrence and magnitude of CP cases (Lee and McPhaden 2010), and these idealized simulations provide a context from which to evaluate potential future impacts on

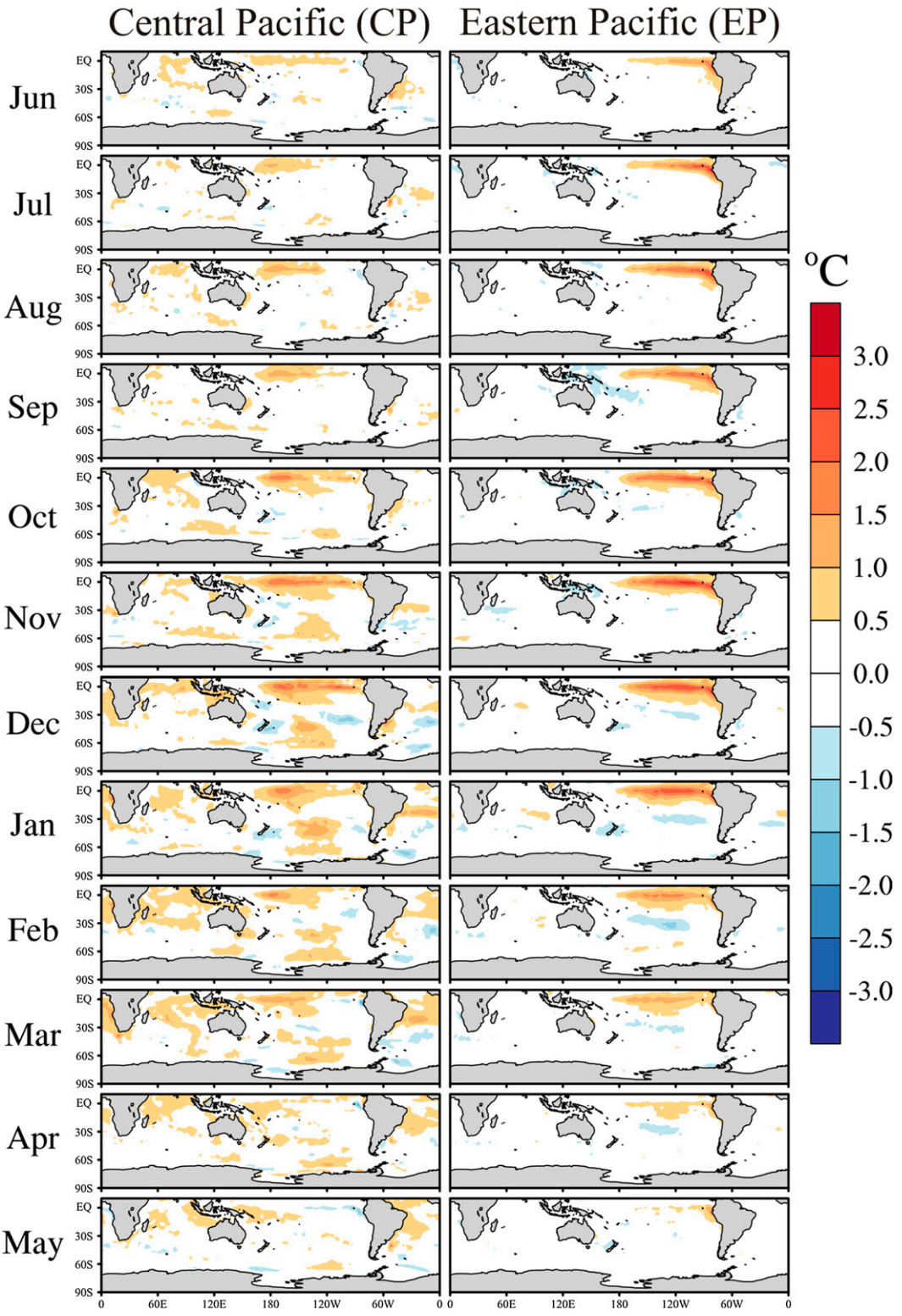

FIG. 2. Monthly composites of SST anomalies (°C) compared to the long-term mean (1950–2010) for both the (left) CP and (right) EP case for $\text{June}_{\text{before}}$–$\text{May}_{\text{after}}$ El Niño maturity, shown only for 10°N–90°S.

atmospheric circulation variability due to changing ENSO variability as well.

Based on the CP and EP composites, the time series of SST anomaly index is calculated for each case using an area-weighted average SST for Niño-4 and Niño-3 regions, respectively. Figure 3 shows the time series of SST anomaly for the CP (blue solid) and EP (red solid) cases. As shown by the spatial anomalies (Fig. 2), the peak season for both cases occurs from late austral spring through summer, decreasing rapidly in the autumn months. Throughout most of the annual cycle, however, the SST anomaly indices for the CP case are less than the magnitudes for the EP case, as these events tend to be weaker than their EP counterparts.

The maximum observed SST anomaly for any month during the 1997 EP El Niño event was 3.5°C. This anomaly is used to scale the idealized cases by setting 3.5°C as the new SST anomaly for the month of November for both cases (Fig. 3). This new anomaly is then divided by the November SST anomaly from each composite case to obtain a scale factor for each flavor. The scale factor is multiplied by the original SST index for all other months for each type. This maintains the annual cycle of the SST anomaly index for each case while increasing the maximum magnitude of both cases. Figure 3 shows the SST anomaly time series for the new CP (blue dashed) and EP (red dashed) idealized simulations as well. Both time series now represent a similar temporal evolution reaching their maximum values in the November with a peak of 3.5°C.

Initially, the scale factor for each case was multiplied by the SST anomalies for all months at all grid points in the model input data. The new resultant field of SST anomalies for the annual cycle showed an increase in the magnitudes of the SST anomalies, with those in the tropical Pacific exceeding +3.0°C for a multitude of grid points. However, both SST anomaly fields were unrealistic at high latitudes with very strong SST gradients. In theory, increasing SSTs in the Southern Ocean without changing the SICs would lead to stronger meridional gradients of temperature and pressure. Thus by the thermal wind relationship, this scenario would increase zonal winds in this area. In fact, a 1-yr sensitivity simulation using globally scaled SSTs as lower boundary conditions lead to zonal wind anomalies in excess of $16.0\,\mathrm{m\,s^{-1}}$ (not shown). Realistically, the increase in SSTs in the Southern Ocean would lead to a decrease in the sea ice surrounding the continent and mitigate the effects from these strong gradients. However, the extent to which this would occur is outside the scope of the current study.

To circumvent this concern, the scale factor is applied to the tropics and subtropics only and relaxed toward the midlatitudes in each hemisphere. The SST anomalies are multiplied by the full scale factor for each case from 30.1°S to 30.1°N. This region not only represents the entire tropical belt where differences between the SST anomalies of the two cases have been described, but it also includes the South Pacific convergence zone (SPCZ; Vincent 1994). The SPCZ is an area associated with high correlation between SAM and SST variability (Ding et al. 2012) and has been demonstrated to be an important pathway for the ENSO teleconnection to the high latitudes of the SH (Chen et al. 1996). Poleward of this area, the original scale factor is decreased by one-fifth of the original value per model latitude. For instance, the SST anomalies along the first model latitude north and south of the full tropical band (31.5°S and 31.5°N) are multiplied by four-fifths of the total scale factor, along the next model latitude (32.9°S and 32.9°N) by three-fifths, and so on until the scale factor is diminished to zero poleward of 35.7°. Thus, this procedure ensures that SST anomalies are consistent with strong cases of each type in the tropics, SPCZ, and SCP without artificially increasing the high-latitude gradients poleward of the scaled region (Fig. 4). Since SST anomalies were present in the Indian and Atlantic Oceans in the original composites of the CP case, the anomalies are much stronger here as well, which is likely to induce additional changes to the dynamics in these tropical ocean basins.

The final step in constructing the SST input data is to add the new scaled monthly SST anomalies for each case to the long-term monthly mean SST for each month. The

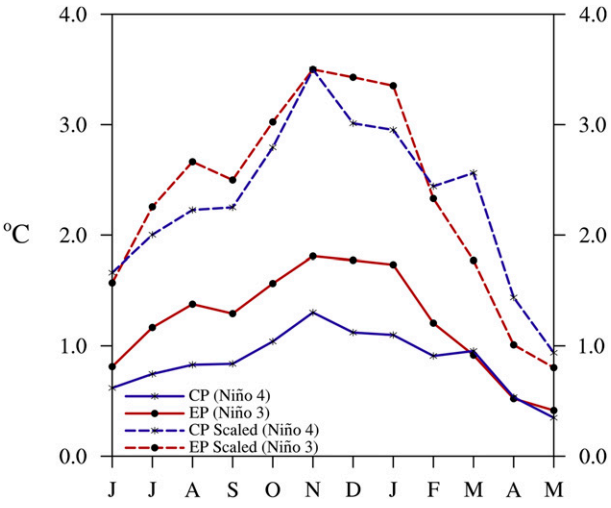

FIG. 3. CP (blue solid) and EP (red solid) SST anomaly time series based on composites in Fig. 2 for $\mathrm{June_{before}}$–$\mathrm{May_{after}}$ El Niño maturity calculated using area-weighted average SSTs within the Niño-4 and Niño-3 boxes, respectively. After scaling the SST anomalies for each case to equal magnitudes, the new CP (blue dashed) and EP (red dashed) SST anomaly indices are also shown.

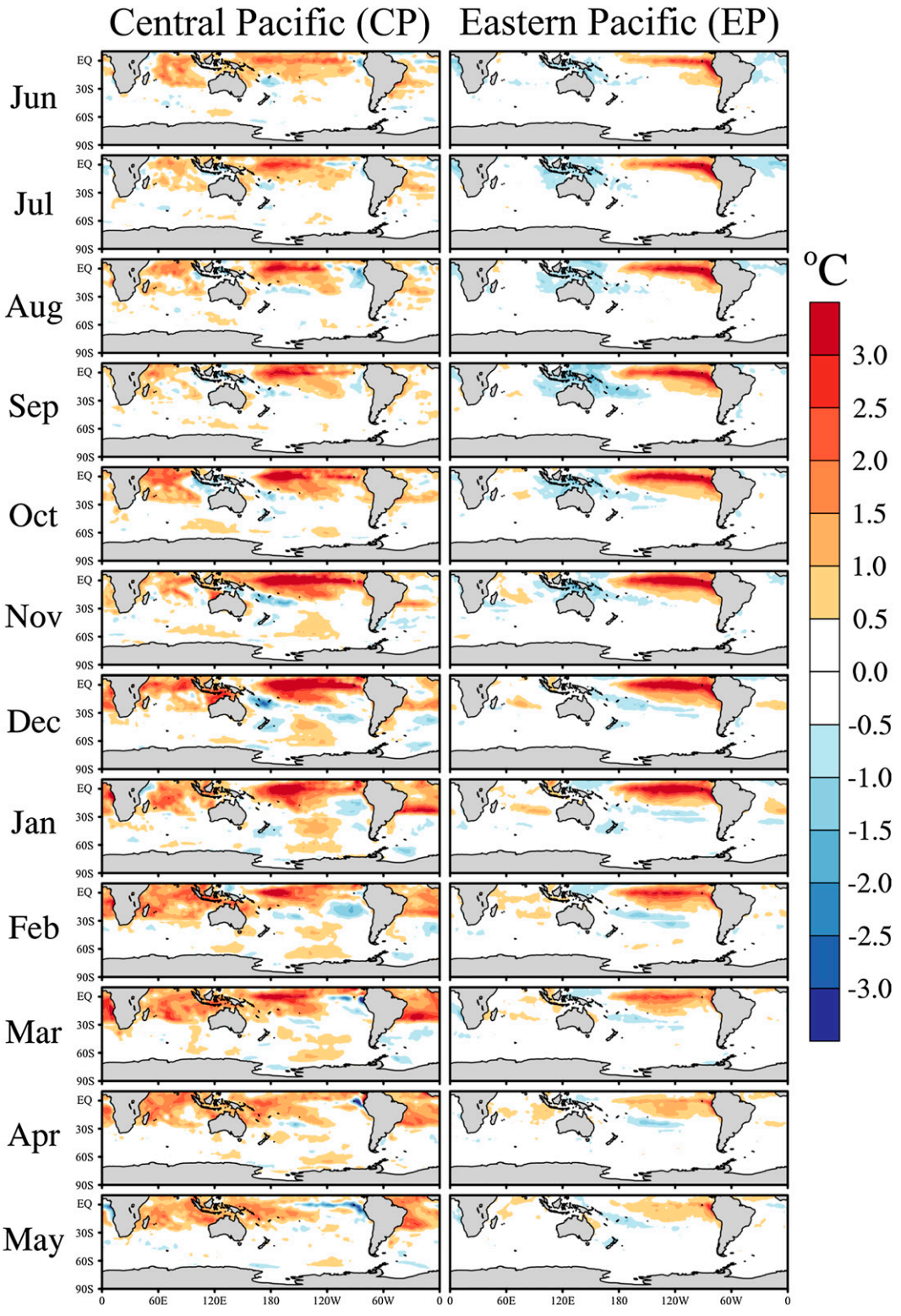

FIG. 4. Monthly composites of SST anomalies (°C) scaled by their respective factor based on the relaxation procedure for the (left) CP and (right) EP cases for $\text{June}_{\text{before}}$–$\text{May}_{\text{after}}$ El Niño maturity, shown only for 10°N–90°S.

TABLE 1. CAM simulations performed in this study. Information includes period of simulation, sea surface boundary conditions, CO_2, and ozone parameters.

Simulation	Period	Lower boundary conditions	CO_2 and ozone
Control	15 yr	Climatological SSTs and SICs	Fixed CO_2 (1990) and climatological ozone
EP	15 yr	Cyclic SSTs from 8 cases of EP El Niños (1950–2010)	Fixed CO_2 (1990) and climatological ozone
CP	15 yr	Cyclic SSTs from 4 cases of CP El Niños (1950–2010)	Fixed CO_2 (1990) and climatological ozone

final product is a 12-month global SST dataset for each flavor (CP and EP) that reflects the tropically scaled anomalies. The model simulations begin in September (using the corresponding cyclic lower boundary conditions) and are run for a total of 15 years and 9 months. The first 9 months are excluded from the final analysis, leaving 15 years of monthly values (June–May) for each El Niño simulation. For comparison, an additional 15-yr simulation (Control) using cyclic SSTs based on the 1981–2010 climatology as lower boundary conditions is also conducted. Annual and seasonal means of atmospheric variables are calculated based on these model results. Table 1 summarizes the model simulations performed for this study.

4. Atmospheric circulation during EP and CP events

El Niño events using the CP and EP criteria that have been observed since 1979 are composited from ERAI. Four CP events (1994–95, 2002–03, 2004–05, and 2009–10) and three EP events (1982–83, 1986–87, and 1997–98) are selected within the ERAI period. While the SSTs for the CAM idealized EP simulation were based on a composite that included five events prior to 1979 and the SST anomalies for the CP simulation were increased to match the CAM EP simulation, analyzing the differences between ERAI CP and EP cases provides a robust basis from which to evaluate the expected differences between the two types of events in the CAM idealized simulations.

Figure 5 shows the general circulation across the SH with annual means of MSLP, geopotential height at 500 hPa (Z500), and zonal wind at 850 hPa (U850) for the ERAI composites (left) and CAM simulations (right). Note that the reduction to sea level over the Antarctic continent introduces errors, but it is plotted here to show the general circulation patterns over the SH. Overall, the ERAI composite MSLP for the EP case (Fig. 5a; solid contours) reflects three high pressure regions anchored in the subtropics of the Atlantic, Indian, and Pacific Oceans. Surrounding Antarctica (~65°S) is the circumpolar trough of low pressure. Between the subtropical highs and the circumpolar trough lies a tight pressure gradient that represents the strong circumpolar westerly winds that flow around the continent. This pressure gradient relaxes in the South Pacific, reflecting a climatological tendency for the winter split jet in this region (Taljaard 1972; van Loon 1972). The subtropical highs for the EP composite are slightly weaker than the climatological mean from ERAI (not shown), which in essence reflects a decrease in the strength of the pressure gradient across the high latitudes of the SH. This suggests weaker zonal flow in high latitudes, which is a known characteristic for mature El Niño events (e.g., Chen et al. 1996). The pattern of MSLP in the EP CAM simulation (Fig. 5b) is similar in structure to ERAI with the placement of the subtropical highs and the band of tighter pressure gradient in the high latitudes. The subtropical high pressure regions are slightly stronger than ERAI with lower pressure (a strong circumpolar trough) near Antarctica resulting in an increase in the meridional pressure gradient between the two regions.

Differences (CP minus EP) for ERAI show that a large portion of the tropics and subtropics from the Atlantic, through the Indian, and into the western Pacific Ocean reflect an MSLP that is 1.0–2.0 hPa lower in the CP composite compared to the EP case (Fig. 5a). The differences between the CP and EP CAM simulations in the tropics are quite similar, with slightly lower MSLP anomalies in the western Pacific (Fig. 5b). This is a signature response of CP events compared to EP types whereby warmer SSTs in the central Pacific basin induce stronger heat fluxes from the ocean surface into the atmosphere, decrease MSLP, and destabilize the atmosphere, which leads to more convection. Higher MSLP in the eastern Pacific extending from the tropics to around 40°S in the ERAI CP composite (significant positive differences as large as +1.0–2.0 hPa) coincides with cooler SSTs that are found near the coast of South America during CP events. CAM once again matches closely the results demonstrated by ERAI with significantly higher MSLP in the tropics eastward of 150°W toward South America in the CP simulation.

At high latitudes, differences displayed by ERAI EP and CP MSLP composites show a wavelike pattern that begins near 40°S, 135°W with significantly higher MSLP extending to significant lower MSLP (−2.0 to −3.0 hPa) near the Drake Passage into the South Atlantic where significantly higher MSLP is once again present. This

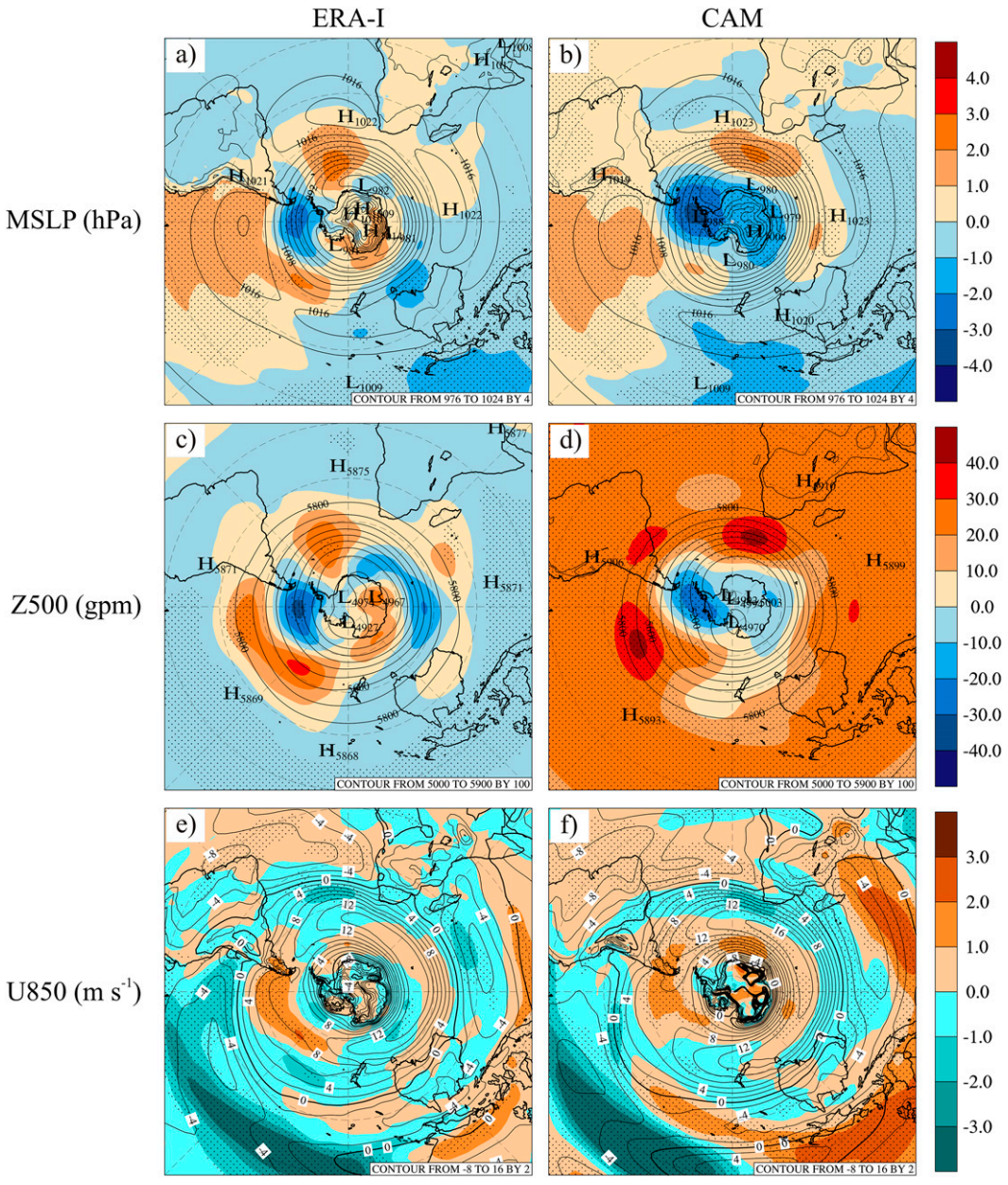

FIG. 5. (left) ERAI composite and (right) CAM simulated annual means of EP (solid contours) for (a),(b) MSLP (hPa), (c),(d) geopotential height at 500 hPa (gpm), and (e),(f) zonal wind at 850 hPa (m s^{-1}). The contour interval for each EP mean variable is provided in the bottom right corner. Differences (CP minus EP) for both ERAI and CAM are color shaded. Differences between CP and EP for each variable for ERAI and CAM are stippled where they are significant at $p < 0.10$.

pattern resembles closely the Pacific–South American (PSA) pattern (Mo and Ghil 1987) which has a center of action in the southeast Pacific near 60°S, 90°W that is excited during ENSO events (Turner 2004). During El Niño events, this region often experiences atmospheric blocking (Renwick 1998). The decrease in MSLP pressure in the CP case in this region provides strong evidence for a weakening in the blocking high that normally accompanies EP El Niño events, with a shift in the high toward the west as indicated by the area of higher MSLP in the SCP. Distinctly, these MSLP differences in ERAI demonstrate significant changes to lower atmospheric circulation in CP compared to EP events. Furthermore, these changes are well modeled by CAM, with increases (smaller than ERAI) in the SCP area and decreases (larger than ERAI) in the Drake

Passage. Some CAM differences between EP and CP flavors do differ with ERAI with the higher MSLP in the Atlantic Ocean shifted toward the east and lower MSLP indicated across the entire Antarctic continent (stronger circumpolar trough), but the overall change in the MSLP field in the high latitudes is well matched by CAM.

Figures 5c and 5d show a similar structure between ERAI and CAM geopotential heights (Z500) in the high latitudes for the EP case (solid contours), respectively. A slight asymmetry about the South Pole is indicated with the lowest heights centered over the Ross Sea. Similar to MSLP, the gradient of heights is strongest throughout the Atlantic and Indian Oceans but weakens in the Pacific sector. Comparing the ERAI EP and CP composites (Fig. 5c), positive differences in heights in the SCP and in the South Atlantic (>40 gpm) along with significantly lower heights near the AP (−20 to −30 gpm) are once again demonstrated. At high latitudes, these differences are similar in CAM but with greater positive differences in the SCP and the eastward shifted area of positive differences in the South Atlantic (Fig. 5d). The negative differences in heights near the Drake Passage are not as great in magnitude as ERAI but remain significant, suggesting a weakened atmospheric block in the EP El Niño favored area of the southeast Pacific. This signifies that the changes to circulation near the surface extend up to the middle troposphere as well, as the equivalent barotropic features of the southern high latitudes are well modeled.

In the tropics, however, ERAI shows decreased heights in the CP case compared to the EP case. This is not mirrored by CAM, which shows significant increases in heights over the same areas. Recall that the magnitudes of the SST anomalies imposed in the CAM CP simulation are much stronger than have yet to be observed for CP events, and the anomalies imposed in the model were forced in the tropics at all longitudes including the Indian and Atlantic Oceans. Warmer SSTs in CAM have generated increased vertical motion and deep convection, which in turn have impacted the geopotential heights throughout the tropics and increased the zonal wind at 500 hPa as well (not shown). However, with the high-latitude differences between EP and CP cases in ERAI being well modeled by CAM, any errors in the midtroposphere in the tropics in CAM have been shown to have minimal impact on the differences between El Niño flavors in the high latitudes. It is also important to remember that the ERAI composites are created using events of all amplitudes for each case, while the amplitudes of each event in CAM have been forced to be strong, which could help explain some of the differences demonstrated between ERAI and CAM in Fig. 5.

Figures 5e and 5f show the EP zonal wind speed ($m\,s^{-1}$; solid contours) for 850 hPa for ERAI and CAM, respectively. The overall structure of the zonal wind in the ERAI EP composite shows that the strongest core of zonal wind (12.0–16.0 $m\,s^{-1}$) extends eastward from the southeast Atlantic Ocean to south of New Zealand between 40° and 50°S. Weaker zonal wind at 850-hPa flow between 40° and 50°S from the date line to the southern tip of South America is a result of the relaxed pressure gradient in the South Pacific compared to the other ocean basins (Fig. 5a). In the subtropics and tropics of the Pacific, the mean easterly trade winds are clearly indicated with magnitudes between −4.0 and −6.0 $m\,s^{-1}$ centered at 20°S, 120°W. In general, the trade winds are weaker (as expected) during the EP El Niño case compared to long-term climatology (not shown).

Comparing the ERAI EP case to the CP case (shaded differences), the trade winds are significantly stronger in the CP composite across the tropical Pacific, indicated by negative differences of −1.0 to −4.0 $m\,s^{-1}$ from 20°S to the equator. This is also expected, as stronger trade winds during CP events help maintain the warm SST anomalies in the central Pacific, mitigating the eastward movement of the warm surface water that is typical of EP events. At higher latitudes, the zonal flow is much stronger between 40° and 50°S in the eastern Pacific and across southern South America. Ashok et al. (2009) suggest that central Argentina experiences an increase in precipitation during CP events due to a southward shift in the storm track compared to EP events. Given the intensification of the MSLP gradient within this area (Fig. 5a), the zonal wind responds by increasing in magnitude. A similar response due to changes in the meridional pressure gradient occur elsewhere including between 50° and 60°S across the South Atlantic and South Indian Oceans.

The structure of the CAM EP simulation is qualitatively similar to ERAI, but the core of the strongest westerly flow is shifted farther to the north in the South Indian Ocean, consistent with a deeper and expanded trough at higher latitudes. As displayed by ERAI, however, CAM shows stronger trade winds in the western tropical Pacific during CP events. The mean westerly zonal wind is also significantly stronger (1.0–2.0 $m\,s^{-1}$) across southern South America in response to the pressure differences across the Drake Passage region. In fact, the zonal wind is stronger at most high latitudes in the CP simulation, which follows the increased pressure gradient in this simulation (more significant than ERAI). In summary, there are clear changes to the atmospheric circulation of the SH demonstrated by the ERAI composites that are well represented in the CAM idealized simulations.

5. Zonal-mean zonal wind and jet streams

Ashok et al. (2009) showed that positive upper-level westerly wind anomalies in the midlatitudes of South America are collocated with enhanced storm-track activity during austral winter for observed El Niño Modoki (CP) events. Figure 6 shows DJF and JJA zonal-mean zonal wind for the CAM Control, EP, and CP simulations, along with differences between the two idealized runs (CP minus EP). First, all three simulations show consistent seasonal variation in zonal-mean zonal wind as the strength the jet stream is strongest in the winter hemisphere as expected. In DJF, the mean westerly jet is located around 200–250 hPa between 40° and 50°S. The position and the magnitude of this jet are similar in all three simulations, indicating little change to the zonal mean jet during the summer in either of the El Niño flavors compared to climatology. Figure 6d shows significantly stronger westerlies (2.0–6.0 m s^{-1}) over tropical latitudes in the CP simulation compared to the EP simulation, while differences less than 1.0 m s^{-1} are present in the high latitudes. During JJA, the magnitude of the jet increases due to a stronger equator-to-pole temperature gradient, with an equatorward shift in the jet that is well captured by both El Niño flavor simulations. For the EP case, the magnitude of this jet is slightly stronger than the Control run while the CP case is weaker. Upper-level tropical westerlies are significantly stronger in the CP simulation than the EP run, which is consistent with the annual differences in geopotential height (Fig. 5d). Warmer SSTs imposed in the tropics for the CP simulation have increased the latent heat flux from the surface and vertical motion (stronger Hadley circulation), resulting in greater zonal momentum in the upper levels of the atmosphere.

Despite the similarity in the equatorward displacement of the jet during JJA, there are important differences between the two flavors during this season. In particular, the CP simulation shows an expansion of the winter jet both poleward and equatorward compared to the EP simulation. This is accompanied by an overall decrease in intensity, indicated by significant changes in the zonal-mean zonal wind near 30°S (Fig. 6h). Larkin and Harrison (2005) showed that the typical EP El Niño effect of heavy precipitation along the coast of Ecuador and northern Peru during winter switches sign during CP events, consistent with a general cooling over the area as well. This relaxation of the STJ with a subtle southward shift in its mean position coinciding with higher surface pressure in the eastern tropical Pacific during CP events (Figs. 5a,b) could also help explain the subtropical precipitation changes.

Focusing on the links between the tropics and high-latitude atmospheric circulation in the Pacific, Fig. 7 shows the austral winter means of the zonal-mean zonal wind averaged for three sectors: the western Pacific (160°E–150°W), eastern Pacific (150°–90°W), and western Atlantic (60°W–0°) between the equator and 90°S. The two Pacific sectors mirror the longitudinal range of the Niño-4 (western) and Niño-3 (eastern) SST indices, while the western Atlantic is also included because of its involvement in changes to the jet streams and association with the ENSO–ADP relationship (Yuan 2004). The split jet stream (Taljaard 1972; van Loon 1972) is evident throughout both basins of the Pacific, with a strong STJ located near 30°S (similar to Fig. 6). A weaker but distinct second maximum in zonal-mean zonal wind, the PFJ, is found near 60°S in all three simulations in the Pacific as well. Evaluating the split jet (300-mb zonal winds) over the South Pacific during a series of ENSO events from 1980 to 1994, Chen et al. (1996) demonstrated an oscillation in the jet strengths during particular ENSO phases. During El Niño, the STJ is amplified while the high-latitude PFJ weakens. Figure 7 shows a stronger STJ in both the EP and CP cases in both basins of the Pacific compared to the Control simulation. In the western Pacific basin, the STJ in the CP case is slightly stronger than in the EP simulation shown by the small but insignificant positive differences near 30°S (Fig. 7d). The PFJs (~60°S) in the high latitudes in both EP and CP El Niños compared to the Control simulation are weaker by 2.0–4.0 m s^{-1}. However, the PFJ is only slightly (insignificantly) stronger near 200 hPa in the western Pacific basin of the CP simulation with respect to the EP case.

Unlike the western Pacific basin, highly significant changes to the STJ between El Niño flavors occur in the eastern basin, with a large triplet of positive–negative–positive differences centered near 30°S (Fig. 7h). This suggests that the evidence in Fig. 6 of a weaker but expanded STJ is largely due to changes in the eastern Pacific. Stronger zonal winds in the tropics during CP events are still present, however, and are likely influenced by the strong SST anomalies induced in the idealized procedure. The slight southward shift in the mean position of the STJ supports earlier findings of an enhanced storm track over central Argentina and weakened activity farther north across in eastern Brazil during El Niño Modoki events (Ashok et al. 2009). In the high latitudes, the CP simulation also shows an overall stronger (insignificant) PJF near 60°S compared to the EP case, opposite to what is expected during a classic El Niño (Chen et al. 1996).

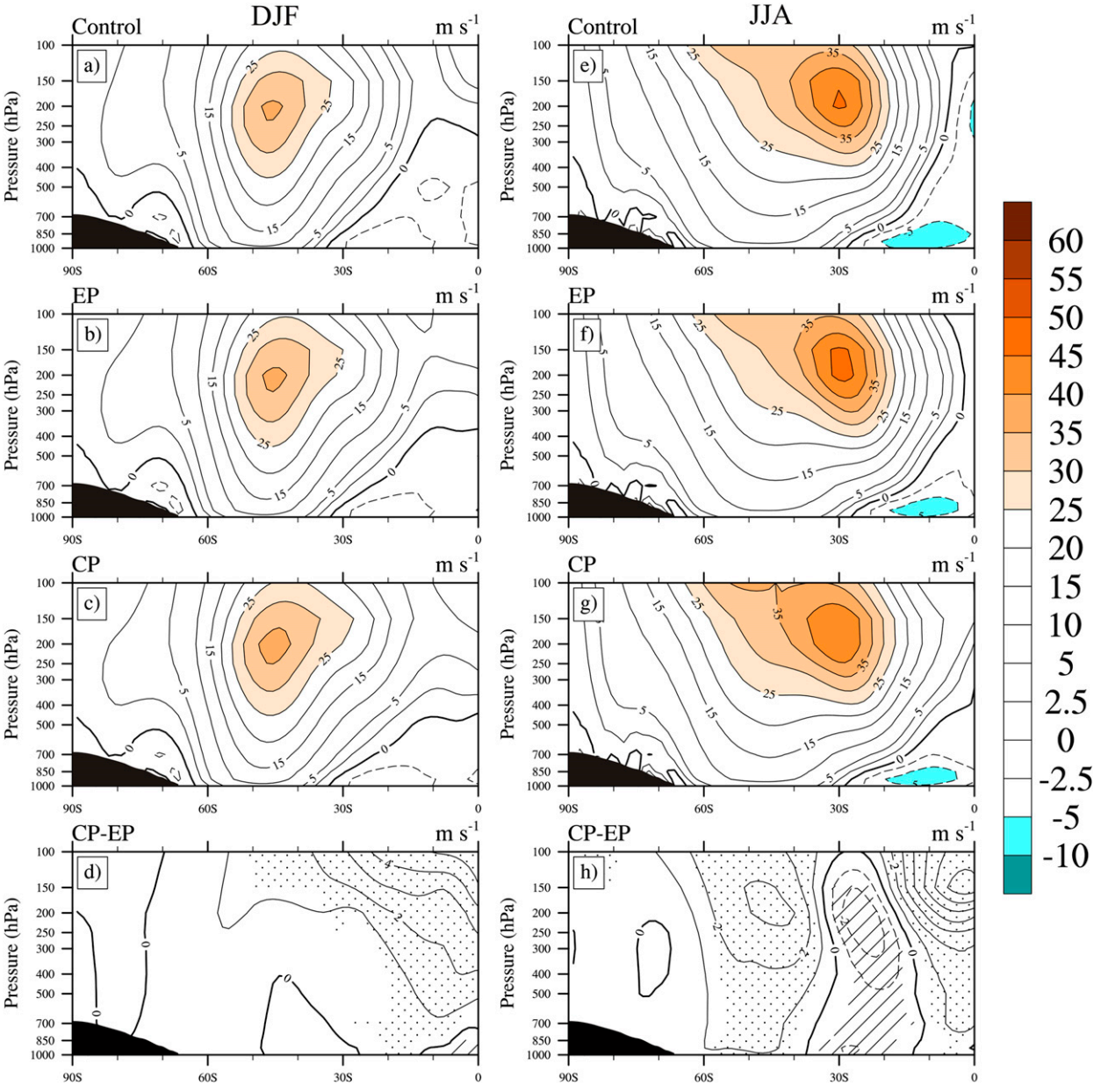

FIG. 6. Seasonal zonal-mean zonal wind for (left) DJF and (right) JJA for the (a),(e) Control, (b),(f) EP, and (c),(g) CP simulations, and (d),(h) the differences between the two simulations (CP minus EP). The means are contoured (solid black lines) on a nonlinear scale to account for much weaker easterly wind in the tropics, and zonal-mean zonal wind is shaded below $-5.0\,\mathrm{m\,s^{-1}}$ and above $25.0\,\mathrm{m\,s^{-1}}$. Differences are contoured by $1.0\,\mathrm{m\,s^{-1}}$ and hashed (negative) or stippled (positive) where they are significant at $p < 0.10$.

Changes in the jet stream are also noted in the western Atlantic Ocean as the split jet ceases near South America, combining into a single jet. Rind et al. (2001) and Yuan (2004) concluded that the storm track in the western South Atlantic shifts poleward in response to a weaker local Hadley circulation during warm ENSO events. Figures 7i and 7j show that during an EP event, the STJ is weaker compared to the Control, and CAM models well the southward shift in the jet in this basin for both types of El Niño. However, the STJ in the CP simulation is stronger than the EP simulation represented by significant differences greater than $2.0\,\mathrm{m\,s^{-1}}$ centered at ~45°S (Fig. 7l). Since the CP EL Niño STJ is weaker in the eastern Pacific and stronger in the western Atlantic compared to EP El Niño, further investigation of the El Niño–ADP relationship as formulated from the classic EP viewpoint is warranted (section 6c).

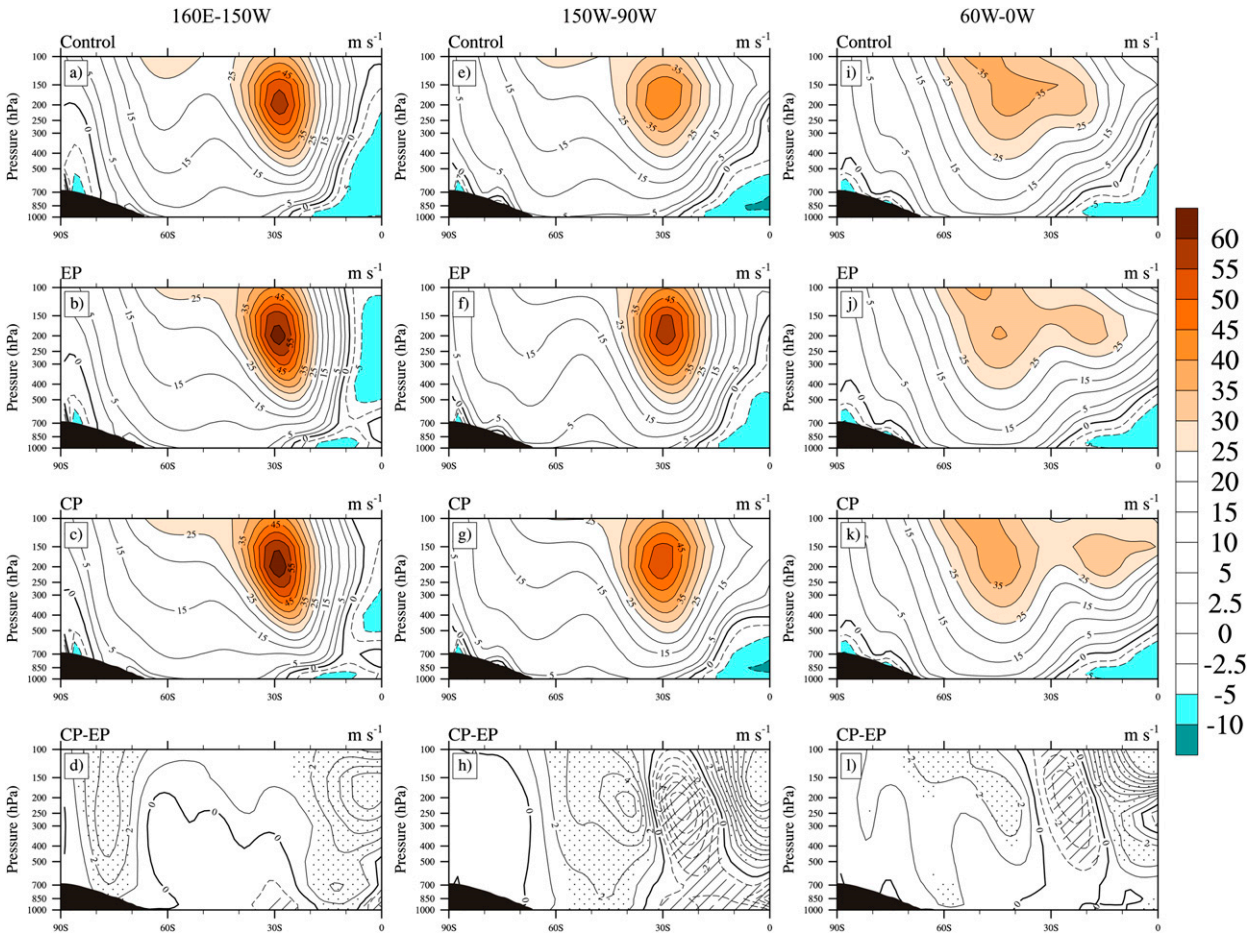

FIG. 7. Austral winter (JJA) zonal-mean zonal wind averaged for three sectors, the (left) western Pacific (160°E–150°W), (middle) eastern Pacific (150°–90°W), and (right) western Atlantic (60°W–0°), for the (a),(e),(i) Control, (b),(f),(j) EP, and (c),(g),(k) CP simulations, and (d),(h),(l) the differences between the two simulations (CP minus EP). The means are contoured (solid black lines) on a nonlinear scale to account for much weaker easterly wind in the tropics, and zonal-mean zonal wind is shaded below $-5.0\,\mathrm{m\,s^{-1}}$ and above $25.0\,\mathrm{m\,s^{-1}}$. Differences are contoured by $1.0\,\mathrm{m\,s^{-1}}$ and hashed (negative) or stippled (positive) where they are significant at $p < 0.10$.

6. Impacts on Southern Hemisphere circulation

To assess potential changes between CP and EP simulated time-averaged departures from the mean flow (PSA), the rotational (streamfunction) and divergent (velocity potential) aspects of the flow are evaluated. Harangozo (2004) showed linkages between the tropics and high latitudes that are strongly tied to nonlinear relationships between convection and upper-level divergence in the tropics. Observations and modeling studies have demonstrated that ENSO variability alters Rossby wave trains and atmospheric circulation across the SH (Karoly 1989; Bromwich et al. 2004; Fogt and Bromwich 2006; Ding et al. 2012), specifically as changes to deep convection impact latent heating during warm and cold phases of ENSO (Lachlan-Cope and Connolley 2006). Similarly, this present analysis supports the idea that CP El Niños shift the PSA pattern westward consistent with the shift in the heating source (Sun et al. 2013), resulting from changes in the upper-level divergence/tropical Rossby wave source region compared to EP events. Additional effects are shown to occur in the SPCZ and at high latitudes including a weakened and westward shift in the blocking regime in the SE Pacific Ocean and a change to the ENSO–ADP teleconnection.

a. Stationary eddies

After removing the zonal mean, the eddy streamfunction emphasizes the large-scale stationary waves that are present in the SH. Figure 8 shows the seasonal means (DJF and JJA) of eddy streamfunction at 200 hPa for the Control, EP, and CP simulations along with the differences (CP minus EP) between the idealized simulations. Negative (positive) streamfunction values in

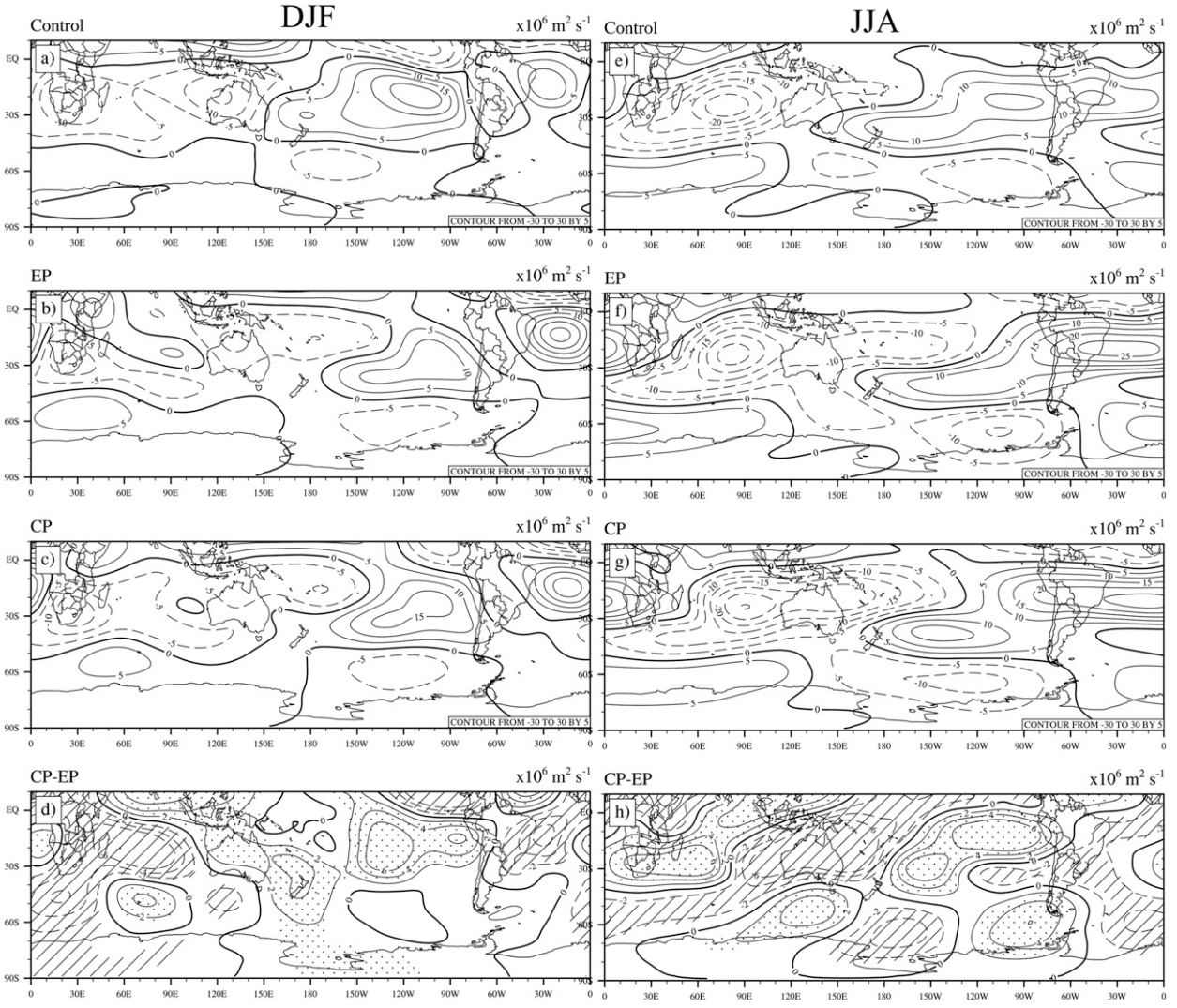

FIG. 8. Seasonal mean 200-hPa eddy streamfunction ($\times 10^6\ m^2\ s^{-1}$) for (left) DJF and (right) JJA for the (a),(e) Control, (b),(f) EP, and (c),(g) CP simulations, and (d),(h) the differences between the two simulations (CP minus EP). The mean eddy streamfunction is contoured from −30.0 to 30.0 by 5.0 ($\times 10^6\ m^2\ s^{-1}$). Differences are contoured by 2.0 and hashed (negative) or stippled (positive) where they are significant at $p < 0.10$.

the SH indicate anticyclonic/counterclockwise (cyclonic/clockwise) flow with increased (decreased) geopotential heights. Expected results are displayed in the Control simulation, with heating-induced anticyclonic flow over the western tropical Pacific and Indian Oceans and cyclonic flow in the eastern tropical Pacific basin associated with the completion of the upper-level portion of the Walker circulation (Figs. 8a,e). This is consistent with the velocity potential at 200 hPa for DJF and JJA as well (Figs. 9a,e), as areas of low velocity potential in the upper levels of the atmosphere indicate regions of strong divergence that coincide with deep tropical convection. Divergent wind flows from areas of low velocity potential toward areas of high velocity potential, and its speed is proportional to the gradient of the velocity potential.

During austral summer, maximum latent heating denoted by the minimum in the velocity potential centered on New Guinea (10°S, 135°E; Fig. 9a) induces anticyclonic flow over northwest Australia (minimum eddy streamfunction; Fig. 8a). Ascent over the warm Amazon during this season is concomitant with upper-level divergence with convergence occurring in the Northern Hemisphere subtropics. During JJA, the maximum heating shifts into the NH and is more intense, leading to a strong gradient of velocity potential and maximum divergent wind across the western Pacific and Indian Oceans (Fig. 9e), which results in a strong

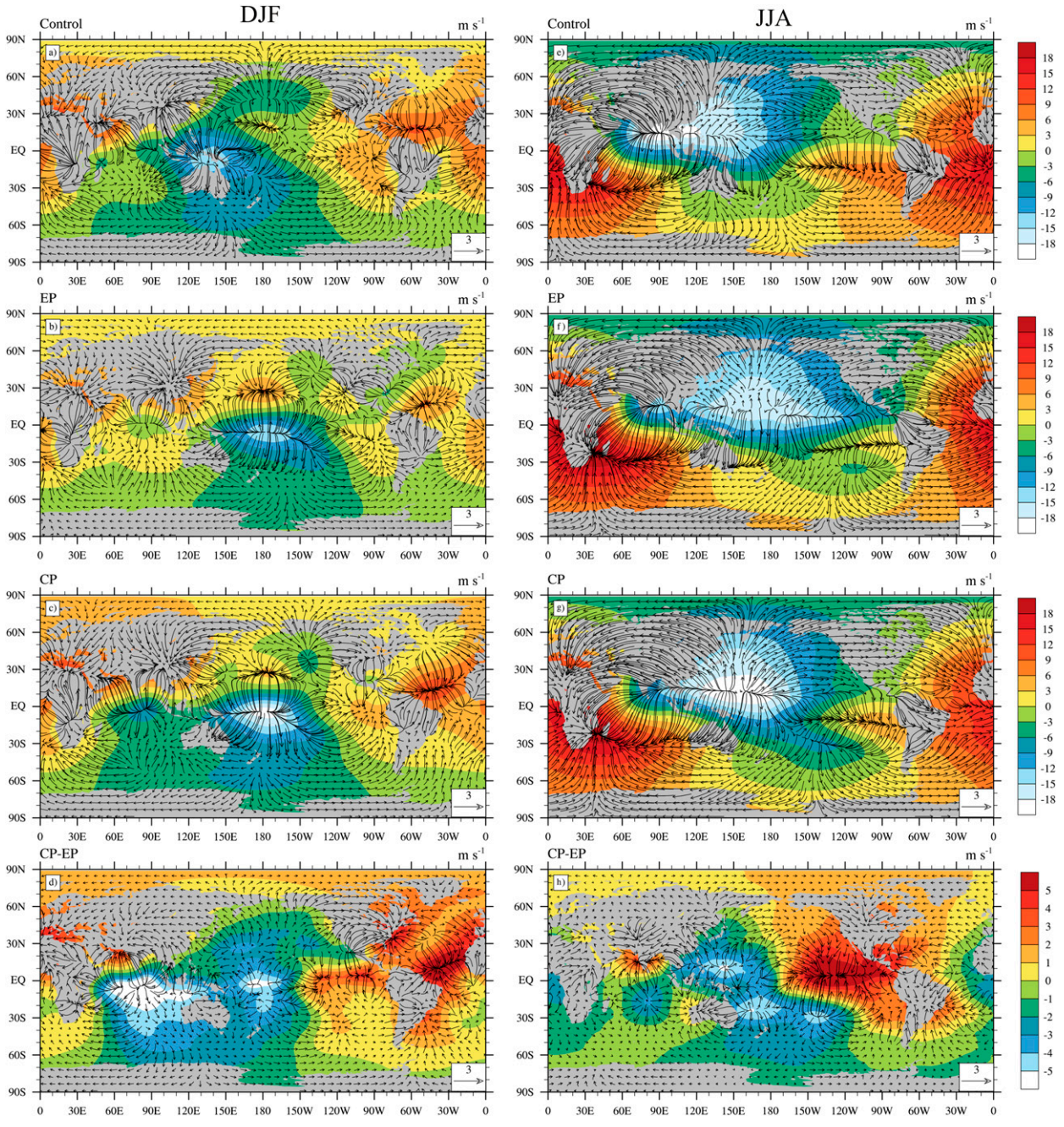

FIG. 9. Seasonal mean 200-hPa velocity potential ($\times 10^6\,m^2\,s^{-1}$; shaded) and divergent wind (black arrows; $m\,s^{-1}$) for (left) DJF and (right) JJA for the (a),(e) Control, (b),(f) EP, and (c),(g) CP simulations, and (d),(h) the differences between the two simulations (CP minus EP).

ridge developing over this region (Fig. 8b). In both seasons, upper-level convergence (maximum velocity potential) is found in the eastern Pacific, a region climatologically associated with cooler SSTs and the descending branch of the Walker circulation, as well as in the eastern South Atlantic associated with descending branch of the Hadley circulation and subtropical high pressure (Fig. 8e).

In higher latitudes, the Control simulation depicts weak anticyclonic flow in the South Pacific (60°S, 180°–150°W) during summer (Fig. 8a) that shifts toward the Antarctic continent during winter (60–75°S, 150°–70°W; Fig. 8e). During JJA, a pattern of negative eddy streamfunction in the western tropical Pacific, positive in the midlatitudes of the South Pacific, and negative once more to the west of the AP resembles the PSA

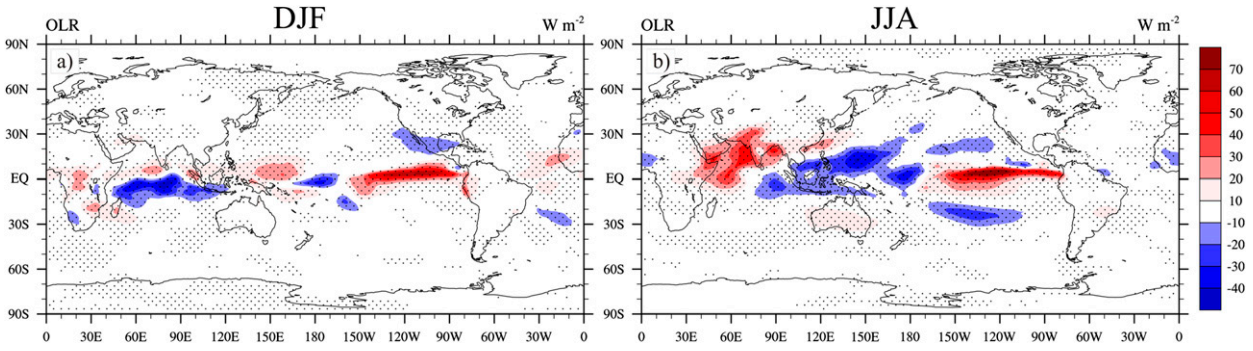

FIG. 10. Seasonal mean outgoing longwave radiation differences (W m^{-2}; CP minus EP) for (a) DJF and (b) JJA. Differences are contoured by 10.0 and stippled where they are significant at $p < 0.10$.

(Fig. 8e), further supporting the theory that even in the absence of an SST-forced response, the PSA is a preferred pattern of variability in the extratropics (Cai and Watterson 2002; Ding et al. 2012). Both the EP and CP simulations show stronger teleconnections during DJF and JJA than the Control simulation (Figs. 8b,c,f,g) in response to an overall weakening of lower-level trade winds and an eastward shift in warm SSTs and convection. This suggests that CAM models well the ENSO amplification of the PSA pattern in the South Pacific.

There are significant differences between the two El Niño simulations, particularly during JJA, a season highly influenced by the El Niño teleconnection. While the structure remains qualitatively similar, Fig. 8h shows greater anticyclonic flow over the western tropical Pacific and Australian continent in the CP simulation, which results in an increase in geopotential height in this region as well (Fig. 5). This is due to increased negative velocity potential north of this region (15°N, 150°E) and an intense gradient of velocity potential resulting in increased divergence across the western tropical Pacific (Fig. 9h). These results support earlier findings by Ashok et al. (2009), who attributed the presence of an anomalous upper-level blocking high over the Australian continent to changes in the divergence in the tropics. Not only is the velocity potential notably more negative in the CP simulation, but its maximum lies mainly west of the date line (Fig. 9g). The change in circulation leads to stronger zonal winds across southern Australia in ERAI (southeast Australia in CAM) (Figs. 5e,f). There is greater cyclonic flow in the eastern tropical Pacific basin that results from a decrease in convection during CP events due to cooler SSTs. Significantly larger velocity potential and strong sinking motion can be found here in the CP simulation, indicating an overall stronger descending branch of the Walker circulation in the eastern Pacific (Fig. 9g).

Similar to the westward shift in the tropical Pacific, Fig. 8h clearly demonstrates a westward shift in the upper-level eddy streamfunction in the South Pacific as well. The differences are significant as anticyclonic flow increases near 65°S, 165°W and decreases near 60°S, 90°W. These results are also supported by changes in MSLP and Z500 in this region (Fig. 5), all indicating tropically induced high-latitude atmospheric circulation changes during CP events.

b. South Pacific convergence zone

A feature of EP El Niño events is a northeastward shift in the SPCZ, an area of high cloudiness and strong convection that is oriented from the western Pacific warm pool (WPWP) near New Guinea southeast toward French Polynesia (30°S, 120°W) (Vincent 1994). Figure 8d (CP − EP) shows slightly more anticyclonic flow in the northwest portion of the SPCZ (0°–10°S, 150°E–180°) during DJF coinciding with a small decrease in the velocity potential (Fig. 9d). Outgoing longwave radiation (OLR) differences (CP − EP) are positive in the WPWP with decreased OLR (cooler cloud tops — deeper convection) in the central Pacific (Fig. 10a). Higher OLR across the eastern tropical Pacific is consistent with increased subsidence in this region (Fig. 5) and a decrease in convection (warmer cloud tops). These results illustrate the twin Walker circulations with a centralized ascending branch in the central Pacific and descending branches on either side (Ashok et al. 2007).

While the SPCZ is well developed during austral summer, it is present year-round. Figure 8h indicates that the SPCZ undergoes a greater change during austral winter, as anticyclonic flow increases across Australia and the western tropical South Pacific. Figure 9h shows an area of decreased velocity potential and increased upper-level divergence near 20°–30°S, 150°–120°W that is concomitant with lower OLR and deeper convection (Fig. 10b). In the eastern tropical Pacific, positive OLR differences are consistent with higher velocity potential and subsidence. After examining the

transition from El Niño to La Niña, Chen et al. (1996) suggested that the high-latitude response in the southeast Pacific during La Niña events could be the result of increased poleward synoptic eddy momentum flux associated with a southwestward shift in the SPCZ. The CP simulation seasonal mean OLR differences between the Control and El Niño simulations (not shown) suggest not only a subtle southwestward shift in the SPCZ during JJA but also a more substantial increase in intensity with colder cloud tops at 15°–30°S, 165°–100°W (Fig. 10b). The anticyclonic feature in the southeast Pacific is reinforced by a preconditioning of the background flow from El Niño and anomalous poleward wave activity that limits wave breaking and excites a negative SAM phase in the high latitudes, unlike a La Niña phase that induces wave breaking and a positive SAM phase (Gong et al. 2010; Fogt et al. 2011). The weakened anticyclone in the CP simulation compared to the EP simulation is inferred to be the result of additional poleward synoptic eddy momentum flux originating from a stronger SPCZ (equatorward wave activity) that is contributing to anticyclonic wave breaking on the equatorward side of the eddy-driven jet. Furthermore, the increase in the magnitude of the anticyclonic flow north of the Ross Sea can be linked to changes in the SPCZ as well. The gradient of the velocity potential in the CP simulation is greater in this region compared to the EP simulation (Figs. 9f,g), indicated by an increase in the divergent wind from the southern extent of the SPCZ and ridge building in the SCP.

In summary, the high-latitude response from the tropical Rossby wave source is anticyclonic (blocking) conditions off the west coast of Antarctica, and Fig. 8h clearly demonstrates a westward shift in the stationary wave pattern throughout the South Pacific including at high latitudes. This shift in the stationary wave pattern imposes changes to the SPCZ, a dynamical mechanism through which tropical variability is translated to the high southern latitudes. An intensified SPCZ during CP events weakens the blocking regime in the southeast Pacific and shifts it toward the west as well, all in response to changes in the upper-level divergence in the tropical Pacific. The dynamical changes are further supported by the evidence in section 4 showing changes to MSLP, Z500, and zonal flow throughout the high southern latitudes (Fig. 5).

c. *The ENSO–ADP relationship*

Together, the significant changes to the SH stationary wave pattern in general, and in the high latitudes in particular, suggest a change to the classic viewpoint of the ENSO–ADP teleconnection (Yuan 2004). The meridional fluxes of heat at 850 hPa and momentum at 200 hPa demonstrate changes to the ENSO–ADP teleconnection (Figs. 11 and 12). During DJF, heat and momentum fluxes are dominated by the zonal flow, as both show minimal poleward and equatorward fluxes at this time in the high southern latitudes. Weak poleward lower-level heat fluxes are evident in the Control simulation north and west of the Ross Sea with equal magnitudes in the EP and CP simulations (although shifted toward the east relative to the Control simulation). Figures 11d and 12d show small differences between the EP and CP simulations in the high latitudes during DJF. These results may support evidence by Song et al. (2011), who show that a strong CP-induced Rossby wave response during austral summer allows the ENSO–ADP connection to persist up until austral winter.

During JJA, however, the ENSO teleconnection and therefore the stationary wave pattern are stronger in the SH with a greater influence on the high southern latitudes. Consequently, the meridional heat and momentum fluxes in the southeast Pacific Ocean associated with the anticyclonic (blocking) flow in this region change, consistent with the eddy streamfunction. For the EP case, blocking off the coast of the AP leads to equatorward fluxes of heat and momentum just west of the AP with stronger poleward fluxes relative to the Control simulation in the Amundsen Sea region (Figs. 11f and 12f). There is a westward shift in the JJA upper-level momentum and lower-level heat fluxes in the CP simulation compared to the EP case (Figs. 11g and 12g), consistent with changes in the stationary wave pattern. Figures 11h and 12h clearly support a weakening in both the equatorward and poleward fluxes associated with a weakening in the blocking regime in the southeast Pacific.

For the South Atlantic, there are differences in the lower-level heat fluxes during the CAM simulations compared to the ENSO events summarized by Yuan (2004). Her analysis was based on five warm ENSO events (post-1980), including the 1986–87 CP–EP mix (Kug et al. 2009) and the 1991–92 CP event. The May–April SSTs averaged for these events showed cool anomalies in the western Atlantic basin that, coupled with changes in the STJ, resulted in less poleward lower-level heat flux in this region. Figure 2 shows that for the monthly SST anomalies of EP events based on 1950–2010, only January has negative SST anomalies less than −0.5°C, as SST anomalies during the other months are close to zero (but mainly positive). During JJA, the small positive SST anomalies in the South Atlantic result in greater poleward lower-level heat fluxes in the EP simulation compared to the Control (Figs. 11e,f), even

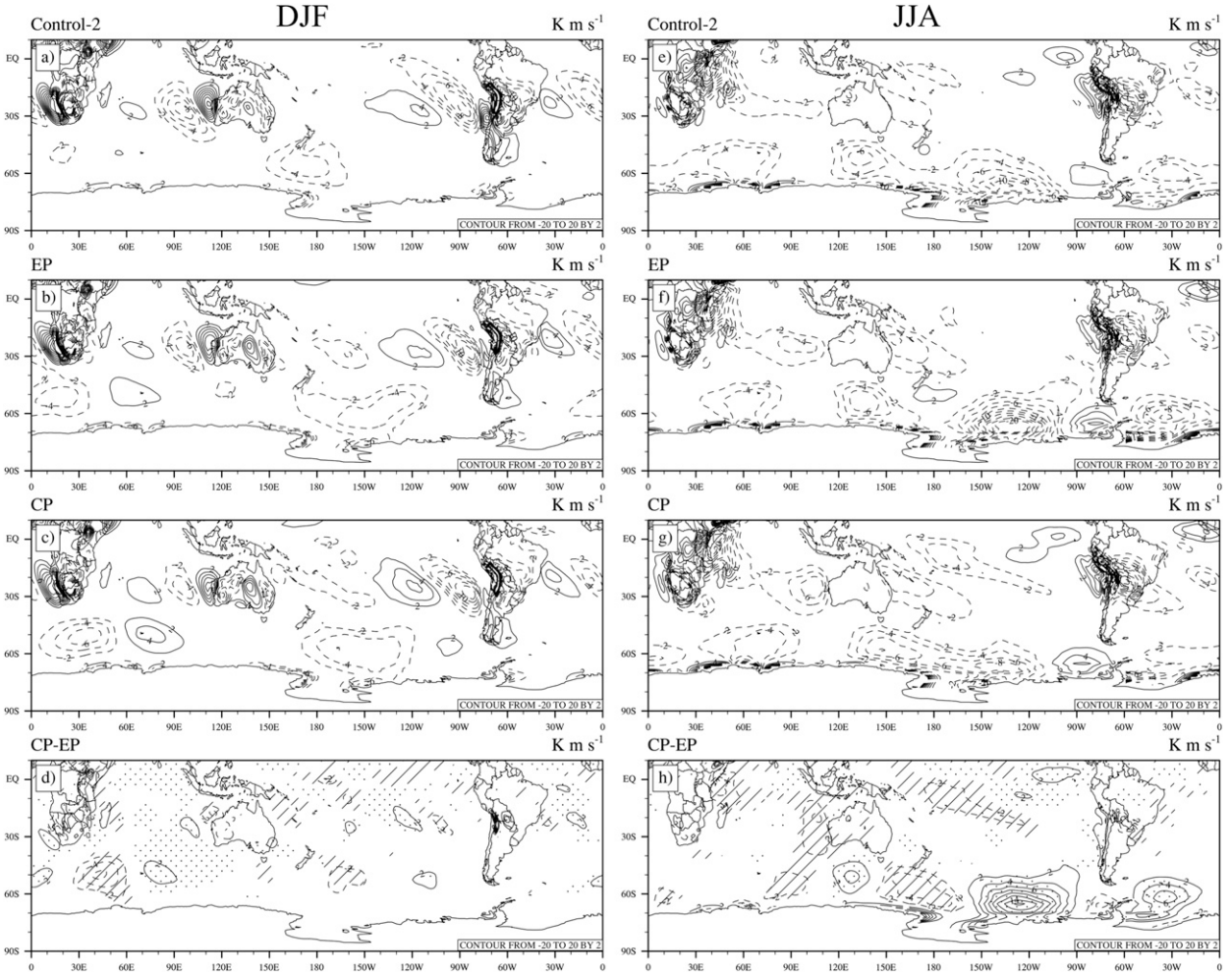

FIG. 11. Seasonal mean 850-hPa meridional flux of heat by stationary eddies (K m s^{-1}) for (left) DJF and (right) JJA for the (a),(e) Control, (b),(f) EP, and (c),(g) CP simulations, and (d),(h) the differences between the two simulations (CP minus EP). The mean heat fluxes and differences are contoured by 2.0. Differences are hashed (negative) or stippled (positive) where they are significant at $p < 0.10$.

though poleward flow (v; not shown) is weaker in the EP simulation. Despite warm SSTs near 30°S in the CP composite (Fig. 2), cool SST anomalies (0° to −0.5°C) are present in the South Atlantic during JJA. These modestly cool SSTs are coupled with greater poleward flow (not shown) in this region, resulting in reduced heat transport toward the Antarctic continent during CP El Niños compared to the EP type (Fig. 11h). Therefore, CAM simulations suggest that during a CP El Niño event, the ENSO–ADP relationship at high latitudes is modified due to a change in upper-level divergence in the tropical Pacific that leads to a westward shift in the stationary wave pattern across the South Pacific, a westward shift and weakening of the lower-level heat and upper-level momentum fluxes off the west coast of Antarctica, and reduced heat transport toward Antarctica in the South Atlantic.

7. Summary and conclusions

This work extends the discussion of CP and EP El Niño impacts to the high southern latitudes. Observed composites of tropical Pacific SSTs reveal that the EP events tend to be much stronger than CP events, although much of the current literature does not account for the differences in the magnitudes of each type of El Niño. From a dynamical point of view, this complicates any comparison made in the structural differences and development of these flavors. Therefore, idealized CAM simulations were conducted using composite SSTs for CP and EP El Niños with lower boundary conditions that were adjusted to equivalent strengths. Changes to high-latitude atmospheric circulation due to altered upper-level dynamics in the tropical Pacific have been directly linked to the location of the warm SST anomalies

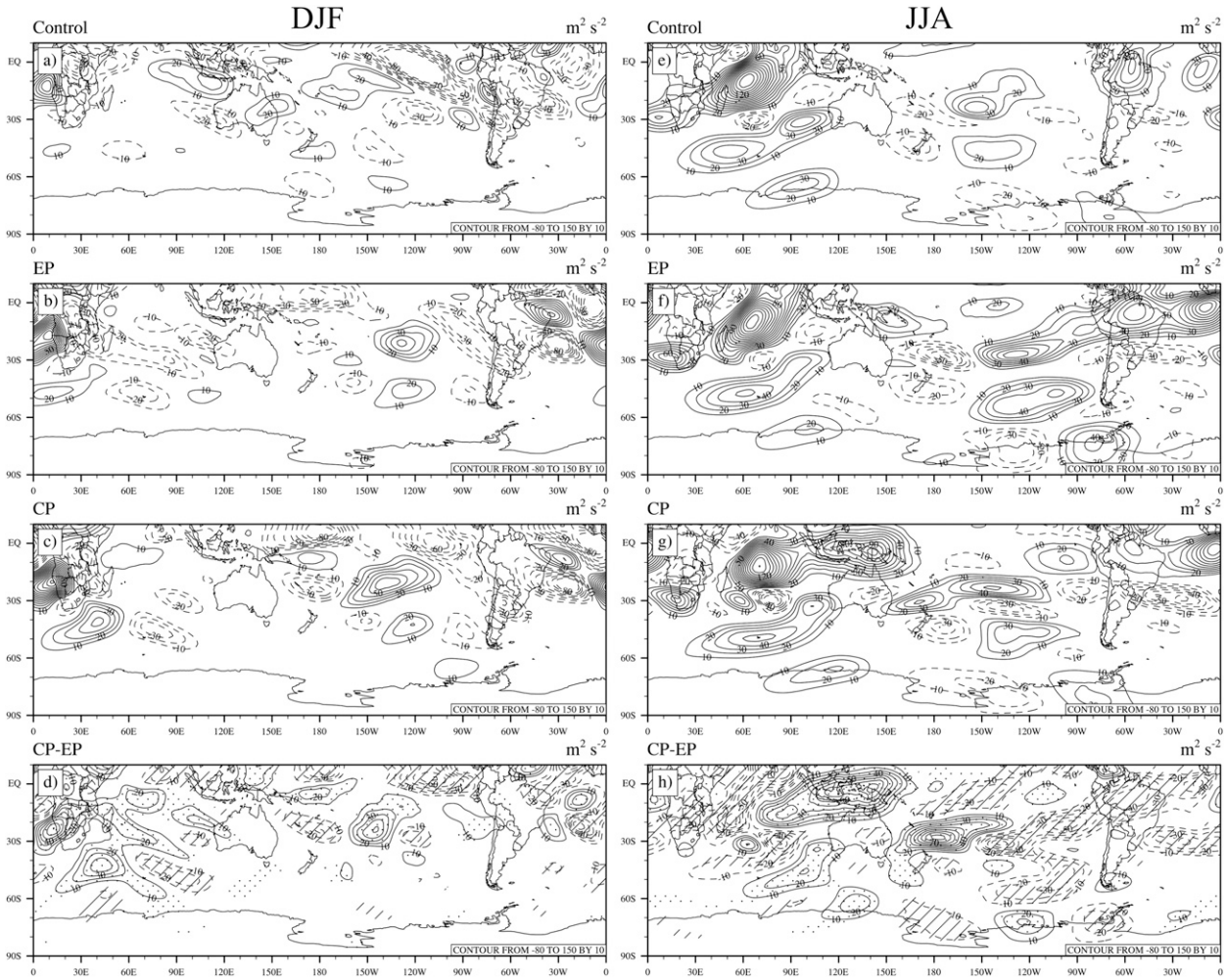

FIG. 12. Seasonal mean 200-hPa meridional flux of momentum by stationary eddies ($m^2 s^{-}2$) for (left) DJF and (right) JJA for the (a),(e) Control, (b),(f) EP, and (c),(g) CP simulations, and (d),(h) the differences between the two simulations (CP minus EP). The mean momentum fluxes and differences are contoured by 10.0. Differences are hashed (negative) or stippled (positive) where they are significant at $p < 0.10$.

and resultant convection associated with each type of El Niño.

Overall, atmospheric circulation changes in CAM due to CP El Niño events match well the patterns demonstrated by ERAI. An increase in anticyclonic flow in the 200-hPa eddy streamfunction over Australia and a southward shift in the STJ across the eastern Pacific basin in CAM verifies previous studies showing CP–EP changes to circulation in the lower latitudes including anomalous blocking over Australia and zonal wind increases at all levels across central Argentina (Ashok et al. 2009). We have extended the analysis of CP–EP changes to atmospheric circulation in the high southern latitudes. Specifically, the PSA stationary wave pattern is altered as lower velocity potential and greater upper-level divergence in the western tropical Pacific during the CP simulation compared to the EP case shifts the initiation of the Rossby wave and resultant wave pattern westward throughout the South Pacific. The SPCZ is more intense during JJA as well, which, coupled with the changes in the Rossby wave source in the tropics, leads to weaker blocking in the southeast Pacific Ocean that is often associated with EP events. Eddy streamfunction analysis shows decreased upper-level anticyclonic flow in the ABS region and a shift toward greater anticyclonic flow in the SCP. A weaker STJ in the eastern Pacific and stronger STJ in the South Atlantic along with differences in the associated high-latitude SST anomalies alter stationary eddy heat and momentum fluxes associated with the ENSO–ADP teleconnection. This implies that the sea ice dipole relationship between the Amundsen and Weddell Seas is altered as well and links changes in the tropical Pacific Rossby wave source region to meridional impacts of the tropics on high-southern latitude atmospheric circulation.

Although SST anomalies were repeated during the simulations to create multiple cases, it is important to point out that these composites are based on relatively few observed CP events. There are also many other questions remaining in the investigation of CP and EP events and their links to high-latitude circulation, including what effects may be specifically attributed to other tropical basins including the Atlantic and Indian Oceans. Likewise, El Niño flavors represent the extremes of a continuum of events. How are the effects similar or different for mixed-flavor events? Additional CAM simulations utilizing observed SSTs from select ENSO flavor events (including La Niñas) will be analyzed in order to elicit further details concerning their development and dynamics.

Acknowledgments. This research was supported by the National Science Foundation (NSF) Grants ATM-0751291 and PLR-1341695. CAM simulations were conducted using the Ohio Supercomputing Center's (https://www.osc.edu/) IBM Cluster 1350 (Glenn Cluster). The authors thank Jialin Lin of the Atmospheric Sciences Program in the Department of Geography at The Ohio State University for his insightful direction on the construction of the lower boundary conditions for the idealized simulations presented in this manuscript.

REFERENCES

Ashok, K., S. K. Behera, S. A. Rao, H. Weng, and T. Yamagata, 2007: El Niño Modoki and its possible teleconnection. *J. Geophys. Res.,* **112,** C11007, doi:10.1029/2006JC003798.

——, C.-Y. Tam, and W.-J. Lee, 2009: ENSO Modoki impact on the Southern Hemisphere storm track activity during extended austral winter. *Geophys. Res. Lett.,* **36,** L12705, doi:10.1029/2009GL038847.

Bracegirdle, T. J., 2013: Climatology and recent increase of westerly winds over the Amundsen Sea derived from six reanalyses. *Int. J. Climatol.,* **33,** 843–851, doi:10.1002/joc.3473.

——, and G. J. Marshall, 2012: The reliability of Antarctic tropospheric pressure and temperature in the latest global reanalyses. *J. Climate,* **25,** 7138–7146, doi:10.1175/JCLI-D-11-00685.1.

Bromwich, D. H., A. J. Monaghan, and Z. Guo, 2004: Modeling the ENSO modulation of Antarctic climate in the late 1990s with the Polar MM5. *J. Climate,* **17,** 109–132, doi:10.1175/1520-0442(2004)017<0109:MTEMOA>2.0.CO;2.

——, J. P. Nicolas, and A. J. Monaghan, 2011: An assessment of precipitation changes over Antarctica and the Southern Ocean since 1989 in contemporary global reanalyses. *J. Climate,* **24,** 4189–4209, doi:10.1175/2011JCLI4074.1.

——, ——, ——, M. A. Lazzara, L. M. Keller, G. A. Weidner, and A. B. Wilson, 2013: Central West Antarctica among the most rapidly warming regions on Earth. *Nat. Geosci.,* **6,** 139–145, doi:10.1038/ngeo1671.

Cai, W., and I. G. Watterson, 2002: Modes of interannual variability of the Southern Hemisphere circulation simulated by the CSIRO climate model. *J. Climate,* **15,** 1159–1174, doi:10.1175/1520-0442(2002)015<1159:MOIVOT>2.0.CO;2.

Capotondi, A., 2013: ENSO diversity in the NCAR CCSM4 climate model. *J. Geophys. Res. Oceans,* **118,** 4755–4770, doi:10.1002/jgrc.20335.

Chen, B., S. R. Smith, and D. H. Bromwich, 1996: Evolution of the tropospheric split jet over the South Pacific Ocean during the 1986–89 ENSO cycle. *Mon. Wea. Rev.,* **124,** 1711–1731, doi:10.1175/1520-0493(1996)124<1711:EOTTSJ>2.0.CO;2.

Dee, D. P., and Coauthors, 2011: The ERA-Interim reanalysis: Configuration and performance of the data assimilation system. *Quart. J. Roy. Meteor. Soc.,* **137,** 553–597, doi:10.1002/qj.828.

Ding, Q., E. J. Steig, D. S. Battisti, and J. M. Wallace, 2012: Influence of the tropics on the southern annular mode. *J. Climate,* **25,** 6330–6348, doi:10.1175/JCLI-D-11-00523.1.

Fogt, R. L., and D. H. Bromwich, 2006: Decadal variability of the ENSO teleconnection to the high-latitude South Pacific governed by coupling with the southern annular mode. *J. Climate,* **19,** 979–997, doi:10.1175/JCLI3671.1.

——, ——, and K. Hines, 2011: Understanding the SAM influence on the South Pacific ENSO teleconnection. *Climate Dyn.,* **36,** 1555–1576, doi:10.1007/s00382-010-0905-0.

Gent, P. R., and Coauthors, 2011: The Community Climate System Model version 4. *J. Climate,* **24,** 4973–4991, doi:10.1175/2011JCLI4083.1.

Gong, T., S. B. Feldstein, and D. Luo, 2010: The impact of ENSO on wave breaking and southern annular mode events. *J. Atmos. Sci.,* **67,** 2854–2870, doi:10.1175/2010JAS3311.1.

——, ——, and ——, 2013: A simple GCM study on the relationship between ENSO and the southern annular mode. *J. Atmos. Sci.,* **70,** 1821–1832, doi:10.1175/JAS-D-12-0161.1.

Harangozo, S. A., 2004: The relationship of Pacific deep tropical convection to the winter and springtime extratropical atmospheric circulation of the South Pacific in El Niño events. *Geophys. Res. Lett.,* **31,** L05206, doi:10.1029/2003GL018667.

Holton, J. R., 1992: *An Introduction to Dynamic Meteorology*. Academic Press, 511 pp.

Hurrell, J. W., J. J. Hack, A. S. Phillips, J. Caron, and J. Yin, 2006: The dynamical simulation of the Community Atmosphere Model version 3 (CAM3). *J. Climate,* **19,** 2162–2183, doi:10.1175/JCLI3762.1.

——, ——, D. Shea, J. M. Caron, and J. Rosinski, 2008: A new sea surface temperature and sea ice boundary dataset for the Community Atmosphere Model. *J. Climate,* **21,** 5145–5153, doi:10.1175/2008JCLI2292.1.

Jacobs, S. S., A. Jenkins, C. F. Giulivi, and P. Dutrieux, 2011: Stronger ocean circulation and increased melting under Pine Island Glacier ice shelf. *Nat. Geosci.,* **4,** 519–523, doi:10.1038/ngeo1188.

Jenkins, A., P. Dutrieux, S. S. Jacobs, S. D. McPhail, J. R. Perrett, A. T. Webb, and D. White, 2010: Observations beneath Pine Island Glacier in West Antarctica and implications for its retreat. *Nat. Geosci.,* **3,** 468–472, doi:10.1038/ngeo890.

Kao, H.-Y., and J.-Y. Yu, 2009: Contrasting eastern-Pacific and central-Pacific types of ENSO. *J. Climate,* **22,** 615–632, doi:10.1175/2008JCLI2309.1.

Karoly, D. J., 1989: Southern Hemisphere circulation features associated with El Niño–Southern Oscillation events. *J. Climate,* **2,** 1239–1252, doi:10.1175/1520-0442(1989)002<1239:SHCFAW>2.0.CO;2.

Kayano, M. T., and R. V. Andreoli, 2006: Relationships between rainfall anomalies over northeastern Brazil and the El Niño Southern Oscillation. *J. Geophys. Res.,* **111,** D13101, doi:10.1029/2005JD006142.

——, ——, and R. A. Ferreira de Souza, 2013: Relations between ENSO and the South Atlantic SST modes and their effects on

the South American rainfall. *Int. J. Climatol.,* **33,** 2008–2023, doi:10.1002/joc.3569.

Kim, W., S.-W. Yeh, J.-H. Kim, J.-S. Kug, and M. Kwon, 2011: The unique 2009–2010 El Niño: A fast phase transition of warm pool El Niño to La Niña. *Geophys. Res. Lett.,* **38,** L15809, doi:10.1029/2011GL048521.

Kug, J.-S., F.-F. Jin, and S.-I. An, 2009: Two types of El Niño events: Cold tongue El Niño and warm pool El Niño. *J. Climate,* **22,** 1499–1515, doi:10.1175/2008JCLI2624.1.

——, J. Choi, S.-I. An, F.-F. Jin, and A. T. Wittenberg, 2010: Warm pool and cold tongue El Niño events as simulated by the GFDL 2.1 coupled GCM. *J. Climate,* **23,** 1226–1239, doi:10.1175/2009JCLI3293.1.

Lachlan-Cope, T., and W. Connolley, 2006: Teleconnections between the tropical Pacific and the Amundsen-Bellinghausens Sea: Role of the El Niño/Southern Oscillation. *J. Geophys. Res.,* **111,** D23101, doi:10.1029/2005JD006386.

Larkin, N. K., and D. E. Harrison, 2005: Global seasonal temperature and precipitation anomalies during El Niño autumn and winter. *Geophys. Res. Lett.,* **32,** L16705, doi:10.1029/2005GL022860.

Lee, T., and M. J. McPhaden, 2010: Increasing intensity of El Niño in the central-equatorial Pacific. *Geophys. Res. Lett.,* **37,** L14603, doi:10.1029/2010GL044007.

——, and Coauthors, 2010: Record warming in the South Pacific and western Antarctica associated with the strong central-Pacific El Niño in 2009–10. *Geophys. Res. Lett.,* **37,** L19704, doi:10.1029/2010GL044865.

L'Heureux, M. L., and D. W. J. Thompson, 2006: Observed relationships between the El Niño–Southern Oscillation and the extratropical zonal-mean circulation. *J. Climate,* **19,** 276–287, doi:10.1175/JCLI3617.1.

Liu, J., X. Yuan, D. Rind, and D. G. Martinson, 2002: Mechanism study of the ENSO and southern high latitude climate teleconnections. *Geophys. Res. Lett.,* **29** (14), doi:10.1029/2002GL015143.

Mo, K. C., and M. Ghil, 1987: Statistics and dynamics of persistent anomalies. *J. Atmos. Sci.,* **44,** 877–902, doi:10.1175/1520-0469(1987)044<0877:SADOPA>2.0.CO;2.

Neale, R. B., J. H. Richter, and M. Jochum, 2008: The impact of convection on ENSO: From a delayed oscillator to a series of events. *J. Climate,* **21,** 5904–5924, doi:10.1175/2008JCLI2244.1.

——, and Coauthors, 2010: Description of the NCAR Community Atmosphere Model (CAM 4.0). NCAR Tech. Rep. NCAR/TN-485+STR, 212 pp.

Nicolas, J. P., and D. H. Bromwich, 2011: Climate of West Antarctica and influence of marine air intrusions. *J. Climate,* **24,** 49–67, doi:10.1175/2010JCLI3522.1.

Peixoto, J. P., and A. H. Oort, 1992: *Physics of Climate*. American Institute of Physics, 520 pp.

Rayner, N. A., D. E. Parker, E. B. Horton, C. K. Folland, L. V. Alexander, D. P. Rowell, E. C. Kent, and A. Kaplan, 2003: Global analyses of sea surface temperature, sea ice, and night marine air temperature since the late nineteenth century. *J. Geophys. Res.,* **108,** 4407, doi:10.1029/2002JD002670.

Renwick, J. A., 1998: ENSO-related variability in the frequency of South Pacific blocking. *Mon. Wea. Rev.,* **126,** 3117–3123, doi:10.1175/1520-0493(1998)126<3117:ERVITF>2.0.CO;2.

——, and M. J. Revell, 1999: Blocking over the South Pacific and Rossby wave propagation. *Mon. Wea. Rev.,* **127,** 2233–2247, doi:10.1175/1520-0493(1999)127<2233:BOTSPA>2.0.CO;2.

Revell, M. J., J. W. Kidson, and G. N. Kiladis, 2001: Interpreting low-frequency modes of Southern Hemisphere atmospheric variability as the rotational response to divergent forcing. *Mon. Wea. Rev.,* **129,** 2416–2425, doi:10.1175/1520-0493(2001)129<2416:ILFMOS>2.0.CO;2.

Reynolds, R. W., N. A. Rayner, T. M. Smith, D. C. Stokes, and W. Wang, 2002: An improved in situ and satellite SST analysis for climate. *J. Climate,* **15,** 1609–1625, doi:10.1175/1520-0442(2002)015<1609:AIISAS>2.0.CO;2.

Rind, D., M. Chandler, J. Lerner, D. G. Martinson, and X. Yuan, 2001: Climate response to basin-specific changes in latitudinal temperature gradients and implications for sea ice variability. *J. Geophys. Res.,* **106** (D17), 20161–20173, doi:10.1029/2000JD900643.

Rodrigues, R. R., R. J. Haarsma, E. J. D. Campos, and T. Ambrizzi, 2011: The impacts of inter–El Niño variability on the tropical Atlantic and northeast Brazil climate. *J. Climate,* **24,** 3402–3422, doi:10.1175/2011JCLI3983.1.

Seager, R., N. Harnik, Y. Kushnir, W. Robinson, and J. Miller, 2003: Mechanisms of hemispherically symmetric climate variability. *J. Climate,* **16,** 2960–2978, doi:10.1175/1520-0442(2003)016<2960:MOHSCV>2.0.CO;2.

Simmons, A. J., and R. Strüfing, 1981: An energy and angular-momentum conserving finite-difference scheme, hybrid coordinates and medium-range weather prediction. ECMWF Tech. Rep. 28, 68 pp.

Song, H.-J., E. Choi, G.-H. Lim, Y. H. Kim, J.-S. Kug, and S.-W. Yeh, 2011: The central Pacific as the export region of the El Niño–Southern Oscillation sea surface temperature anomaly to Antarctic sea ice. *J. Geophys. Res.,* **116,** D21113, doi:10.1029/2011JD015645.

Sun, D., F. Xue, and T. Zhou, 2013: Impact of two types of El Niño on atmospheric circulation in the Southern Hemisphere. *Adv. Atmos. Sci.,* **30,** 1732–1742, doi:10.1007/s00376-013-2287-9.

Taljaard, J. J., 1972: Synoptic meteorology of the Southern Hemisphere. *Meteorology of the Southern Hemisphere, Meteor. Monogr.,* No. 35, Amer. Meteor. Soc., 139–211.

Trenberth, K. E., 1997: The definition of El Niño. *Bull. Amer. Meteor. Soc.,* **78,** 2771–2777, doi:10.1175/1520-0477(1997)078<2771:TDOENO>2.0.CO;2.

Turner, J., 2004: The El Niño–Southern Oscillation and Antarctica. *Int. J. Climatol.,* **24,** 1–31, doi:10.1002/joc.965.

van Loon, H., 1972: Wind in the Southern Hemisphere. *Meteorology of the Southern Hemipshere, Meteor. Monogr.,* No. 35, Amer. Meteor. Soc., 87–99.

Vincent, D. G., 1994: The South Pacific convergence zone (SPCZ): A review. *Mon. Wea. Rev.,* **122,** 1949–1970, doi:10.1175/1520-0493(1994)122<1949:TSPCZA>2.0.CO;2.

von Storch, H., and F. W. Zwiers, 1999: *Statistical Analysis in Climate Research*. Cambridge University Press, 484 pp.

Wilson, A. B., 2013: Using the NCAR CAM 4 to confirm SAM's modulation of the ENSO teleconnection to Antarctica and assess changes to this interaction during various ENSO flavor events. Ph.D. dissertation, The Ohio State University, 296 pp.

Yeh, S.-W., J.-S. Kug, B. Dewitte, M.-H. Kwon, B. P. Kirtman, and F.-F. Jin, 2009: El Niño in a changing climate. *Nature,* **461,** 511–514, doi:10.1038/nature08316.

Yu, J.-Y., and S. T. Kim, 2010: Three evolution patterns of Central-Pacific El Niño. *Geophys. Res. Lett.,* **37,** L08706, doi:10.1029/2010GL042810.

——, M.-M. Lu, and S. T. Kim, 2012: A change in the relationship between tropical central Pacific SST variability and the extratropical atmosphere around 1990. *Environ. Res. Lett.,* **7,** 034025, doi:10.1088/1748-9326/7/3/034025.

Yuan, X., 2004: ENSO-related impacts on Antarctic sea ice: A synthesis of phenomenon and mechanisms. *Antarct. Sci.,* **16,** 415–425, doi:10.1017/S0954102004002238.